# Wave-bottom interaction and extreme wave statistics due to shoaling and de-shoaling of irregular long-crested wave trains over steep seabed changes

**Jie Zhang [1], Michel Benoit†[1]**

[1]Aix Marseille Univ, CNRS, Centrale Marseille, Institut de Recherche sur les Phénomènes Hors-Equilibre (IRPHE, UMR 7342), 13013 Marseille, France

(Received xx; revised xx; accepted xx)

The formation of abnormal (extreme) waves in coastal areas can be triggered by wave-seabed interaction, in particular by steep bottom changes. As an incident equilibrium sea-state passes over a submerged step or bar, non-equilibrium dynamics appears locally and forces the sea-state to a new, finite-depth equilibrium along with strong non-Gaussian statistics and intensified occurrence probability of large waves. In this study, the experimental case Run 3 reported by Trulsen et al. [J. Fluid Mech. **882**, R2 (2020)] has been investigated numerically with a fully nonlinear model. Furthermore, as both shoaling and de-shoaling effects exist in the setup with a bar-profile bottom, an additional simulation with a step-profile bottom is performed to isolate the de-shoaling effects. The model is proven excellent by the confrontation of the measurements and simulated results in both time and spectral domains. Strong non-Gaussian behaviour of the sea-state is highlighted after the up-slope transition by combining spectral and bispectral analysis, and characteristic parameters. With a harmonic extraction approach, we show evidence that both second- and third-order effects triggered by the non-equilibrium dynamics significantly enhance the local kurtosis and occurrence of extreme waves. The statistics of kinematics shows the asymmetry of the wave field evolves somewhat independently in horizontal and vertical directions. By comparing the simulations of bar- and step-profile cases, we find the de-shoaling process is responsible for the upstream modulation of nonlinear and dispersive parameters, and the enhancement of kurtosis of both horizontal and vertical velocity and horizontal acceleration over the down-slope area.

**Key words:**

## 1. Introduction

In deep-water conditions, abnormal high waves, also called "freak" (or "rogue") waves are frequently explained by the self-modulation property of nonlinear wave trains (Benjamin & Feir 1967; Onorato *et al.* 2005; Toffoli *et al.* 2013). Sudden appearance of these extreme waves can lead to catastrophic consequences (Dysthe *et al.* 2008). As ocean waves propagate toward nearshore areas, they are affected by finite water depth effects and sea bottom variations. The transformation and deformation of sea-states due to non-uniform depth are subject to complex dynamics involving numerous physical processes, including

† Email address for correspondence: benoit@irphe.univ-mrs.fr

shoaling and refraction due to seabed gradients, reflection and diffraction due to islands or seabed irregularities, wave-wave interactions, dissipation due to bottom friction and depth-induced breaking in shallow-water areas (see e.g. Goda 2010).

The propagation of wave trains over strong depth variations is another mechanism for explaining the occurrence of abnormal waves in coastal areas (Kharif & Pelinovsky 2003). In such a situation, the rapid changes of the water depth result in strong modifications to the local wave spectrum, pushing it out of the equilibrium (or near-equilibrium) shape it had offshore. After the depth transition, the sea-state rapidly settles to a new equilibrium compatible with the shallow water depth. The sea-state transition areas could be prone to higher probability of occurrence of extreme waves (see e.g. Trulsen *et al.* 2012; Ma *et al.* 2015; Viotti & Dias 2014; Ducrozet & Gouin 2017). The occurrence probability of these extreme waves can be characterised by statistical parameters of the sea-state, especially kurtosis carrying information on the tail of the statistical distributions of wave crest elevation and wave height (see Janssen 2003; Mori & Janssen 2006). It is thus of interest to investigate the variations of statistical parameters due to rapid depth transitions in coastal areas.

Trulsen *et al.* (2012) reported experiments with long-crested irregular waves propagating over a shoal and showed that local maximum of skewness, kurtosis and an enhanced probability of occurrence of extreme waves could be observed near the end of the slope. Katsardi *et al.* (2013) conducted experimental tests with mild bottom slopes, and concluded that the slope effect can be ignored when the gradient is milder than 1:100. Kashima & Mori (2019) experimentally tested several types of bottom profiles. They suggested that the third-order nonlinearity in the deeper region, where the sea-state is modulationally unstable, provokes aftereffects influencing the downstream sea-state in the shallower region. The amplified extreme waves due to depth changes remain until the surf zone. In the work of Zhang *et al.* (2019), experiments with a sloping bottom were conducted in a large-scale flume, showing similar variation trends of statistical parameters as in Trulsen *et al.* (2012). Strong local triad wave-wave interactions were detected around the end of the slope via Fourier-based bi-spectral analysis. For experiments of uneven bottoms with bar-profile, Ma *et al.* (2015) focused on the parameters including groupiness, skewness, and kurtosis. They found that the appearance of high waves was positively correlated with groupiness. Chen *et al.* (2018) used wavelet-based bi-spectrum to characterise nonlinear triad interactions, showing that nonlinear triad interactions become stronger for steeper slopes.

The local variations of the statistical parameters are related to the significant dynamical responses occurring due to depth changes. Trulsen *et al.* (2020) conducted a series of experiments with a bar-profile bottom with rather steep slopes at both sides. They identified two regimes with different dynamical responses, and showed that the dynamical responses of the sea-states depend on the relative water depth $k_p h$ in the shallower region (where $h$ denotes the water depth and $k_p$ the local peak wave-number). In the so-called "shallower regime" with $k_p h$ being lower than a threshold, significant enhancements of the statistical parameters and the probability of extreme wave occurrence are expected. On the contrary, for waves that enter into a sufficiently deep nearshore zone (the so-called "deeper regime"), the responses of statistical parameters are trivial and do not exhibit large enhancements. The threshold was found to be $k_p h = 1.3$ in their work, but it may vary for different conditions. Trulsen *et al.* (2020) also observed that the local maximum of kurtosis of the horizontal fluid velocity was achieved at a different position from that of the kurtosis of the free surface elevation.

From the modelling viewpoint, Zeng & Trulsen (2012) used the cubic nonlinear Schrödinger equation (NLS) with variable coefficients, to study the influence of variable

bottom profile on the probability of occurrence of extreme waves. In their cases with intermediate water depth and slowly varying bottom, particular patterns of the spatial structure of skewness and kurtosis were identified. Non-equilibrium statistics due to depth transitions may extend beyond the end of the slope. No localised enhancement of statistics over the sloping area was observed, implying the cases considered in Zeng & Trulsen (2012) belong to the "deeper regime". Gramstad *et al.* (2013) used a Boussinesq model with improved linear dispersion properties, while Kashima *et al.* (2014) used a standard Boussinesq model with an artificial correction of nonlinearity to reproduce the experiments of Trulsen *et al.* (2012). Both studies further considered different bottom profiles and observed significant increases of skewness, kurtosis, and probability of occurrence of extreme waves around the end of the sloping bottom areas. Sergeeva *et al.* (2011) studied the dynamical responses of the sea-state over uneven bottom within the framework of the Korteweg-de Vries equation with variable coefficients. They showed that for sea-states with stronger nonlinearity, the dynamical responses are more pronounced. Although these numerical studies insightfully demonstrated the effects of non-equilibrium dynamics due to non-uniform bathymetry, they were inevitably constrained by the limited capability of the approximate models in representing nonlinear and dispersive wave properties over a broad range of relative depth conditions.

Fully nonlinear and dispersive models are therefore of interest in studying the sea-state adaptations due to depth variations. The first study in this path was done by Viotti & Dias (2014) through simulations of the free-surface Euler equations using a spectral method. They showed the non-equilibrium responses in a local region increase for stronger depth variations, resulting in intensified extreme wave occurrence. Ducrozet & Gouin (2017) considered directional sea-states propagating over a sloping bottom with the High-Order Spectral (HOS) method (Dommermuth 2000; Gouin *et al.* 2016), showing the non-negligible influence of the directional spreading on the sea-state dynamics. Zheng *et al.* (2020) adopted a fast multipole boundary element method to simulate the experiments of Trulsen *et al.* (2012), and tested more parameter choices. They discussed the effects of different parameters including wave steepness, relative water depth, and bottom gradient on the length of latency, which is defined as the distance between the end of shoal and the position where skewness and kurtosis reach their maximum. By conducting harmonic extraction with phase-inversion technique, Zheng *et al.* (2020) concluded that the second-order terms are responsible for the local changes of statistical properties. However, with the two-phase technique, the separated 'linear term' is in fact a summation of first-, third-, and higher odd order harmonics. The 'second-order' terms consist of the second-, fourth-, and higher even order harmonics. In their work, no further discussion was made on the possible effects of these ignored harmonics, especially the third harmonic. In the work of Zhang *et al.* (2019), a fully nonlinear and dispersive potential flow code, whispers3D, was adopted and compared with a Boussinesq-type model introduced by Bingham *et al.* (2009). The good agreement with the measurements conducted in a large wave flume demonstrated the high accuracy of whispers3D.

The main objective of the present work is to investigate the non-equilibrium dynamics and associated statistics of irregular long-crested wave trains propagating over non-uniform bathymetry by considering one particular test (Run 3) of the experiments reported in Trulsen *et al.* (2020) (for the sake of brevity, this paper will be referred to as TRJR20, and the chosen case as R3 hereafter). The submerged trapezoidal bar in TRJR20 consists of a rather steep slope at both ends. Our aim is to achieve a better understanding of the non-equilibrium dynamics induced by both shoaling and de-shoaling processes. The effects of the first up-slope transition are discussed on the basis of the in-depth analysis of the original experimental measurements and additional data extracted

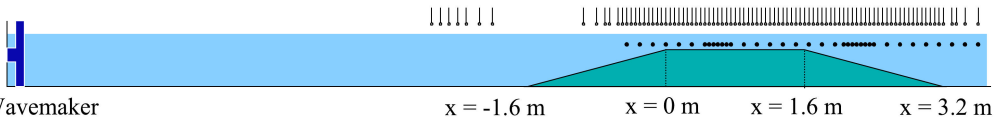



FIGURE 1. Sketch of bottom profile and locations of the wave gauges, adapted from figure 2 of Trulsen *et al.* (2020), and reproduced with permission from Cambridge University Press.

from the simulations. The effects of the de-shoaling area with increasing water depth are analysed by simulating a variation of the R3 case with a step-like profile.

The remainder of this article is laid out as follows. In §2, the configurations of the chosen experimental case of TRJR20 and the numerical modelling approach are recalled. Then in §3, the original R3 case is reproduced with extra information extracted and analysed. In §4, the variation case of R3 with a step-profile is simulated. By comparing with the R3 simulation, the effects of the de-shoaling zone are isolated. In §5, the main findings from this work are summarised, with perspectives for further investigations.

## 2. Experimental configuration, numerical modelling and analysis methods

### 2.1. *Experimental setup used by TRJR20*

Details on the description of the experimental facility and tested conditions can be found in the original paper of TRJR20. Here, only their test labelled 'Run 3' is considered, whose data set contains free surface elevation signals measured at 91 locations along the wave flume, and horizontal velocity signals measured at 37 different locations and at an elevation $z_0 = -0.048$ m below the still water level (SWL). The schematic view of the flume is shown in figure 1. It should be noticed that, compared to figure 2 in TRJR20, the origin of the horizontal axis is placed here at the end of the up-slope. We selected this R3 test mainly for two reasons: on the one hand, R3 belongs to the 'shallower regime', with the shoal being shallower than the threshold $k_p h = 1.3$ suggested in TRJR20. The kurtosis of the free surface elevation was enhanced up to 4.2 at the beginning of the shallower flat region in R3, which is the most pronounced amplification among the cases in TRJR20. On the other hand, R3 is the only case with horizontal velocity measurements: this is of interest for a deeper analysis of the wave transformation processes and the validation of orbital velocities computed with the model.

The incident irregular long-crested wave train is generated from a JONSWAP spectrum. The experimental conditions are controlled by four parameters: the water depth $h_1$ in the deeper flat region, the incident significant wave height $H_{m_0} = 4\sqrt{m_0}$, where $m_0$ is the zeroth moment of the spectrum, the peak period $T_p$ (or peak frequency $f_p$) and the peak enhancement factor $\gamma$ of the JONSWAP spectrum $S(f)$ in the following form:

$$S(f) = \frac{\alpha_J g^2}{(2\pi)^4} \frac{1}{f^5} \exp\left[-\frac{5}{4}\left(\frac{f_p}{f}\right)^4\right] \gamma^{\exp\left[-(f-f_p)^2/\left(2\sigma_J^2 f_p^2\right)\right]}, \tag{2.1}$$

where $g$ denotes the gravitational acceleration, $\alpha_J$ the wave height adjustment factor, and $\sigma_J$ the spectral asymmetric parameter ($\sigma_J = 0.07$ if $f \leqslant f_p$ and $\sigma_J = 0.09$ if $f > f_p$).

The key parameters of R3 are listed in table 1. The non-dimensional parameters include relative water depth $\mu = k_p h$, steepness $\epsilon = k_p a_c$, and Ursell number $U_r = \epsilon/\mu^3$. The characteristic wave amplitude is $a_c = \sqrt{2}\sigma$, with $\sigma$ being the standard deviation of the surface elevation: $\sigma^2 = \left\langle (\eta - \langle\eta\rangle)^2 \right\rangle = m_0$, where $\langle\cdot\rangle$ denotes the time-averaging

| Run | $T_p$ (s) | $\gamma$ | Deeper region | | | | | Shallower region | | | | |
|---|---|---|---|---|---|---|---|---|---|---|---|---|
| | | | $h_1$ (m) | $\mu_1$ | $H_{m_0}$ (m) | $\epsilon_1$ | $Ur_1$ | $h_2$ (m) | $\mu_2$ | $H_{m_0}$ (m) | $\epsilon_2$ | $Ur_2$ |
| 3 | 1.1 | 3.3 | 0.53 | 1.85 | 0.025 | 0.031 | 0.0049 | 0.11 | 0.64 | 0.025 | 0.052 | 0.1918 |

TABLE 1. Key parameters of the experimental case reported as Run 3 in Trulsen *et al.* (2020).

operator. The non-dimensional numbers are computed and averaged in the first deeper region (marked by subscript 1) and over the shoal crest (marked by subscript 2). Two misprints for $\mu$ and $Ur$ in the deeper region were detected in table 1 of TRJR20 and are corrected here. The signals in R3 are recorded over a duration of 90 min (equivalent to about 4,900 waves with period $T_p$) with a high sampling frequency $f_s = 125$ Hz. No breaking event was reported by TRJR20 during R3 test.

### 2.2. *Outline of the mathematical and numerical model*

We assume the fluid is inviscid and incompressible, the flow is irrotational and the surface tension is negligible. A two-dimensional Cartesian coordinate system $(x, z)$ is considered. As shown in figure 1, the origin of x-axis along the flume is set at the beginning of the shallower region, and $z$-axis points upward with $z = 0$ at SWL. The equations governing the fluid motion in a domain with a free surface $z = \eta(x, t)$ and a variable bottom profile $z = -h(x)$ are:

$$\nabla^2\phi = 0 \quad \text{for} \quad -h(x) \leqslant z \leqslant \eta(x,t), \tag{2.2}$$

$$\eta_t + \phi_x\eta_x - \phi_z = 0 \quad \text{on } z = \eta(x,t), \tag{2.3}$$

$$\phi_t + \frac{1}{2}\left(\nabla\phi\right)^2 + g\eta = 0 \quad \text{on } z = \eta(x,t), \tag{2.4}$$

$$h_x\phi_x + \phi_z = 0 \quad \text{on } z = -h(x), \tag{2.5}$$

where $\phi(x, z, t)$ denotes the velocity potential, $\nabla$ is the gradient operator ($\nabla\phi \equiv (\phi_x, \phi_z)^T$) and subscripts denote partial derivatives.

The free surface boundary conditions (2.3) and (2.4) are expressed as functions of free surface variables $\eta(x, t)$ and $\tilde{\phi}(x, t) \equiv \phi(x, z = \eta(x, t), t)$, as (Zakharov 1968):

$$\eta_t = -\tilde{\phi}_x\eta_x + \tilde{w}\left(1 + \eta_x^2\right), \tag{2.6}$$

$$\tilde{\phi}_t = -g\eta - \frac{1}{2}\tilde{\phi}_x^2 + \frac{1}{2}\tilde{w}^2\left(1 + \eta_x^2\right), \tag{2.7}$$

where $\tilde{w}(x, t) \equiv \phi_z(x, z = \eta(x, t), t)$ is the vertical component of the velocity at the free surface. To determine the temporal evolution of $\eta$ and $\tilde{\phi}$, one should evaluate $\tilde{w}$ from $(\eta, \tilde{\phi})$, which is known as the Dirichlet–to–Neumann (DtN) problem. The DtN problem is of fundamental importance for the Zakharov formulation, and various approaches have been discussed (see e.g. Dommermuth 2000; Gouin *et al.* 2016; Madsen *et al.* 2006; Bingham *et al.* 2009; Belibassakis & Athanassoulis 2011; Papoutsellis *et al.* 2018).

In whispers3D, the DtN problem is solved by using a spectral approach in the vertical direction, following Tian & Sato (2008) and Yates & Benoit (2015). This code has been validated for numerous conditions (see Raoult *et al.* 2016; Zhang *et al.* 2019; Simon *et al.* 2019), showing excellent performance for the prediction of wave propagation together with acceptable computational burden. The modelling approach of whispers3D has been presented in Yates & Benoit (2015) and Raoult *et al.* (2016) and is briefly recalled here.

First, a change of vertical coordinate is introduced, with a new vertical variable:

$$s(x,z,t) = \frac{2z + h^-(x,t)}{h^+(x,t)}, \tag{2.8}$$

where $h^{\pm}(x,t) = h(x) \pm \eta(x,t)$. The physical domain in $(x,z,t)$ space with variable bottom and free surface boundaries $z = -h(x)$ and $z = \eta(x,t)$, is mapped into a rectangular domain in $(x,s,t)$ space with two fixed boundaries at $s = \pm 1$.

The nonlinear potential water wave problem (2.2–2.5) is then reformulated in the $(x,s,t)$ space with $\varphi(x,s(x,z,t),t) \equiv \phi(x,z,t)$. Using the set of Chebyshev polynomials of the first kind $T_n(s), n = 0,1,...,N_T$ as an expansion basis for $s \in [-1,1]$, the potential is approximated in the transformed domain as:

$$\varphi(x,s,t) \approx \varphi_{N_T}(x,s,t) = \sum_{n=0}^{N_T} a_n(x,t) T_n(s), \tag{2.9}$$

where the coefficients $a_n(x,t), n = 0,1,...,N_T$, are now the main unknowns.

The approximated potential $\varphi_{N_T}$ in (2.9) is inserted into the governing equations composed of the Laplace equation, a Dirichlet boundary condition with $\varphi_{N_T}(x, s = 1, t) = \tilde{\phi}(x,t)$ on the free surface, and the bottom boundary condition expressed in the $(x,s)$ domain. This problem is then solved by using the so-called Chebyshev-tau method outlined by Tian & Sato (2008). The spatial derivatives are evaluated using finite difference schemes applied with stencils composed of $N_{sten}$ nodes. The value of $N_{sten}$ is specified by the user to control the order of accuracy. At each time step, the solution of the problem is the set of coefficients $a_n, n = 0,1,...,N_T$ at each abscissa. With these $a_n$ coefficients, the horizontal velocity $u = \phi_x$ and the vertical velocity $w = \phi_z$ can be evaluated as:

$$u(x,z,t) \approx \frac{\partial \varphi_{N_T}}{\partial x} + \frac{\partial \varphi_{N_T}}{\partial s}\frac{\partial s}{\partial x} = \sum_{n=0}^{N_T} a_{n,x} T_n + \frac{h_x^- - s h_x^+}{h^+} \sum_{n=1}^{N_T} a_n T_{n,s}, \tag{2.10}$$

$$w(x,z,t) \approx \frac{\partial \varphi_{N_T}}{\partial s}\frac{\partial s}{\partial z} = \frac{2}{h^+} \sum_{n=1}^{N_T} a_n T_{n,s}. \tag{2.11}$$

At the free surface, $\tilde{w}$ is obtained by taking $s = 1$ in (2.11), and the DtN problem is solved. To march equations (2.6–2.7) in time, an explicit Strong-Stability-Preserving third-order Runge–Kutta (SSP-RK3) scheme (Gottlieb 2005) is used. In whispers3D, no particular assumption is made on the level of dispersion or nonlinearity of the wave train. Furthermore, no extra assumption on the bottom profile is required. The model is thus considered powerful in describing wave dynamics over arbitrary variable bottom profiles. One can balance accuracy and efficiency via a proper choice of the parameters $N_T$, $N_{sten}$, and numerical step sizes in space ($\Delta x$) and time ($\Delta t$). The incident wave train is imposed on the left boundary of the numerical tank and damped on the right boundary using the relaxation zone technique (Bingham & Agnon 2005). Linear wave-making theory is used, which is applicable for the present study as justified in the next subsection.

### 2.3. *Numerical setup and solution validation*

The effective computational domain, excluding the two relaxation zones, is 6.3 m long, from $x = -2.7$ m to 3.6 m. The generation zone ends at $x = -2.7$ m, i.e. at the position of the first wave probe. The measured signal at this probe was imposed as the incident wave train in the simulations. The relaxation zones are 5.4 m long each, which is roughly 3 peak wavelengths in the deeper region. In figure 2, the schematic view of the numerical

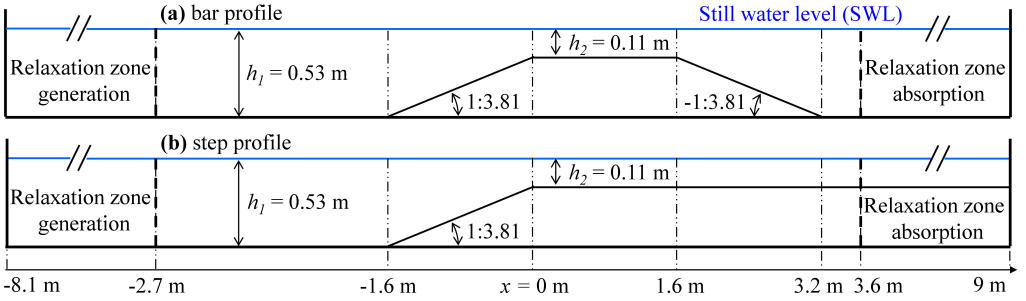



FIGURE 2. Sketch of model setup and bottom profiles adopted in simulations with whispers3D, (*a*) R3-bar profile (identical to the experiment of TRJR20) and (*b*) modified R3-step profile without de-shoaling area.

wave tank for the original R3-bar case is shown in panel (a), and its variation for the R3-step case in panel (b).

The simulations lasted 90 min, as in the experiment. After a convergence study on space and time discretizations (not shown here), $\Delta x = 0.01$ m and $\Delta t = 0.01$ s were selected. With this choice, the Courant–Friedrichs–Lewy number, defined as $\mathrm{CFL} = L_p \Delta t/(T_p \Delta x)$, is approximately 1.64 in the deeper region and 0.97 in the shallower region. Similarly, convergence tests showed that $N_T = 7$ and $N_{sten} = 5$ provide high accuracy.

The variance density spectra of both measured and simulated free surface elevation at probe 1 ($x = -2.7$ m) are shown in figure 3, with the target JONSWAP spectrum of R3 experiment superimposed as reference. The spectrum measured at probe 1 ($x = -2.7$ m) is similar to the target spectrum specified to drive the wave-maker (located at $x = -12.38$ m), with no super-harmonic peaks (i.e. at $2f_p$, $3f_p$, etc.) appearing in the spectrum. It indicates that nonlinear wave-wave interactions remained weak for waves propagating from the wave-maker to probe 1. In figure 3(b), wave energy in the low-frequency (LF) range, defined by $f \in [0, 0.5f_p]$, can be observed in the measured spectrum, but the energy level is very low. The generation of LF modes could be related to wave-wave interactions, intrinsic modes of the flume, and reflected waves which are not effectively damped in the experiment. The low energy level of LF modes at probe 1 indicates that the absorption of the wave energy in the experiment was rather effective in the LF range and that the natural modes were not markedly excited. Such observations support the application of linear wave-making theory to simulate the R3 case.

The measured signal at probe 1 was decomposed into 38,588 harmonic components in the range $[0.4f_p, 5f_p]$. By using linear superposition of these components, the driving signals were computed at left end of the domain and at nodes located in the generation zone. The good agreement between the simulated and measured spectra at probe 1, shown in figure 3, confirms the validity of the linear wave generation method. Only some minor differences are observed, i.e. the magnitude of the spectral peak seen in figure 3(a) and the amplitudes of LF modes in figure 3(b). The former is acceptable because the slight overestimation of the simulated spectral density is limited to a very narrow range $[0.95f_p, 1.05f_p]$, but the averaged energy in a slightly broader range $[0.9f_p, 1.1f_p]$ shows similar values for both spectra. The latter differences are of secondary importance since the LF energy in both simulation and experiment is very low compared to the main part of the spectrum.

The submerged bar provokes some reflection of the incident wave train. As no indication of reflection intensity given in TRJR20, a reflection analysis was undertaken here, using an extension of the least square method of Mansard & Funke (1980) applied to the

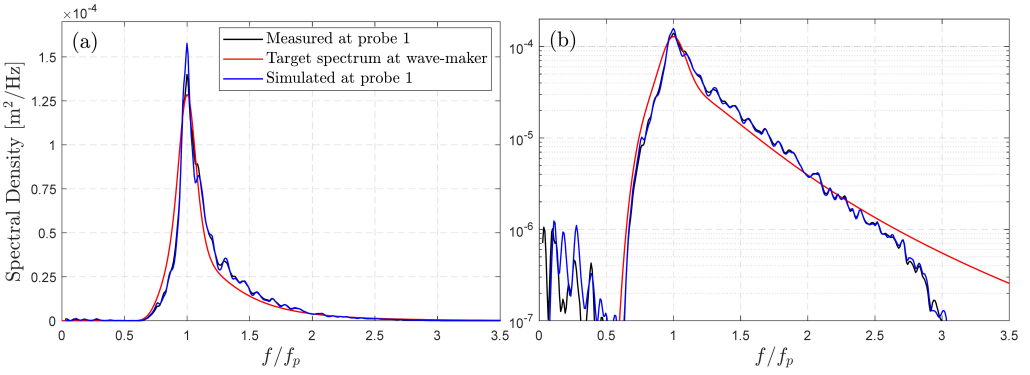



FIGURE 3. Incident variance spectral density of free surface elevation at probe 1 ($x = -2.7$ m) shown in both linear scale (panel *a*) and logarithmic scale (panel *b*). As a reference, the target JONSWAP spectrum imposed at the wave-maker ($x = -12.38$ m) in the experiment is superimposed.

first 7 probes, located before the submerged bar, from $x = -2.7$ m (probe 1) to $-2.0$ m (probe 7). Note that the spatial arrangement of these probes is not optimal for the reflection analysis: for probes 1-5, the distance between two successive probes is 0.10 m, for probes 5-7, it is 0.15 m. The spectral variations of the reflection coefficient $C_r(f)$ for each frequency component $f$ could nevertheless be assessed for both the experiment and simulation of R3 case. The analysis showed that $C_r(f)$ takes values below 10% in the most energetic range around the peak frequency ($0.75 < f/f_p < 1.5$), with very good correspondence between experiment and simulation. For $f > 1.5f_p$, experimental values of $C_r(f)$ are slightly larger than the ones from the simulation. Below $0.75f_p$, $C_r(f)$ takes larger values, confirming that longer waves are more prone to reflection, but the agreement between experiment and simulation remains quite good. Representative values of the reflection coefficient, defined as $\bar{C}_r = H_{m0,ref}/H_{m0,inc}$ with subscripts 'ref' and 'inc' representing reflected and incident respectively, are 8.9% for the experiment and 6.8% for the simulation. It indicates that the reflection is low (below 10%), in both experiment and simulation.

It should be mentioned that dissipation is not considered in the current simulations. Due to the limited size of the effective computation domain, the differences resulting from dissipation are meant to be of secondary significance. The simulated velocity components are recorded at the same positions as for the horizontal ones in R3 experiment.

To demonstrate qualitatively the high fidelity of the simulation, snapshots of the normalised measured and simulated free surface elevation signals are compared at 16 positions along the wave flume in figure 4. The time window, covering the last 30 s of the run, is shifted according to probe positions and the local group velocity $C_g(f_p) = \mathrm{d}\omega/\mathrm{d}k$. It can be seen that the agreement between the simulation and measurements is excellent all over the domain, even after running nearly 90 min of simulation. Only some minor differences are observed. A small phase shift develops for some waves as they propagate towards the end of the flume: the simulated signal gradually moves ahead of the measurements. This could be explained by the ignored dissipation effect in the simulation: without dissipation, the simulated sea-state is of slightly higher energy, with some waves having slightly larger amplitudes. Due to nonlinear dispersion, the phase and group velocity are larger for waves with higher amplitudes, resulting in this small phase shift with the measurements.

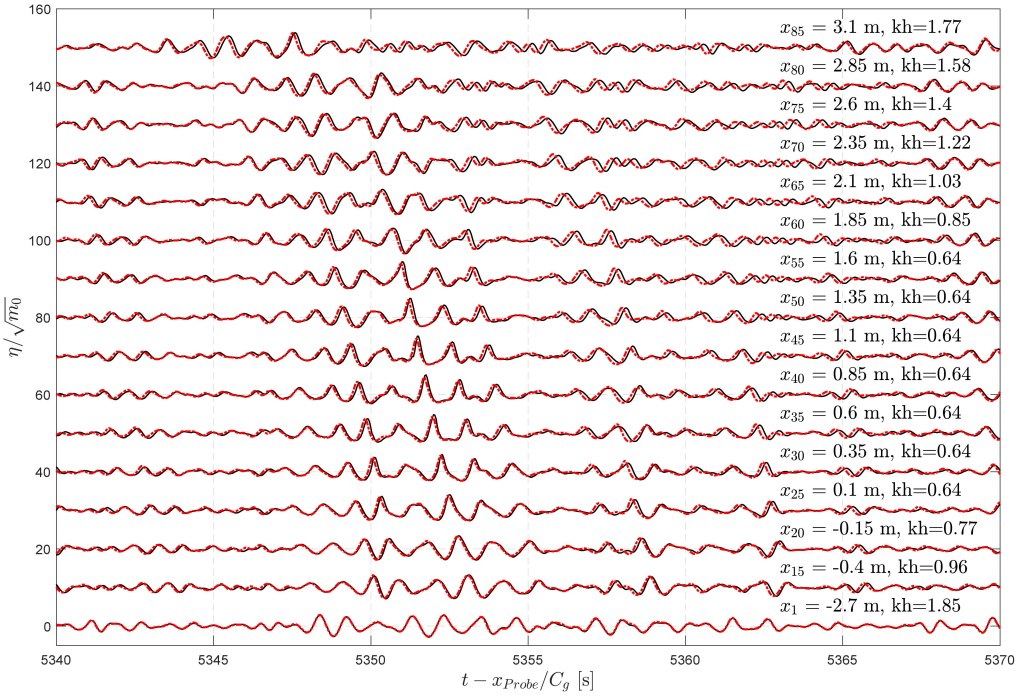



FIGURE 4. Comparison between experimental measurements (black solid lines) and numerical simulation (red dashed lines) of the normalised free surface elevation recorded at 16 positions along the wave flume (probe positions and the corresponding local relative water depths are indicated above each curve). Each of the time series is shifted vertically with an offset of 10 for the sake of clarity.

### 2.4. *Statistical, spectral and bispectral analysis approaches*

To analyse the wave transformation processes, four conventional analysis approaches are applied: (i) analysis of characteristic wave parameters, (ii) spectral (Fourier) analysis, (iii) bi-spectral (Fourier-based) analysis, and (iv) statistical analysis. Since these analysis techniques are commonly used, the formulations and definitions of notations are reported in appendix A, and we mention below only specific aspects.

Regarding (i), eight non-dimensional parameters are selected to characterise the spatial evolution of the sea-state. The nonlinearity is characterised by the normalised significant wave height $H_{m_0}/H_{m_0,inc}$, steepness parameter $H_{m_0}/\hat{L}_p$ (where $\hat{L}_p$ is the wavelength related to the peak frequency $\hat{f}_p$ evaluated with the method of Young (1995), see (A 3)), skewness $\lambda_3$ and kurtosis $\lambda_4$ of several kinematic variables (free surface elevation, orbital velocities and accelerations), and the asymmetry parameter computed from bispectrum. The subscript 'inc' denotes the incident wave characteristic given in table 1. The dispersion parameters include the peakedness parameter $Q_p$, and the normalised local peak frequency $\hat{f}_p/f_{p,inc}$. As a balance of nonlinearity and dispersion, the Benjamin–Feir (B–F) index is considered, with two definitions $\mathrm{BFI}_{S06}$ and $B_s$ applicable for different relative depth conditions. The parameter definitions and related formulations are provided in appendix A.1 Regarding (iii), the bispectral analysis includes both bispectrum $B(f_1, f_2)$ and bicoherence $b^2(f_1, f_2)$. The spectral and bi-spectral analysis approaches are described in appendix A.2 Regarding (iv), the statistical distributions of crest-to-trough wave heights $H$ and free surface elevation $\eta$ are considered to characterise

the deviation of the sea-state from the Gaussianity. The experimental and simulated distributions are compared with the Gaussian distribution for $\eta$ and the theoretical model of Boccotti (2000) for $H$. The distributions of $\eta$ and $H$ are given in appendix A.3.

### 2.5. *Harmonic separation method*

In addition, a harmonic separation method is adopted here. The idea of group inversion allows decomposing the wave group into fundamental components, and was first adopted by Baldock *et al.* (1996) to study focused wave groups in deep-water. Assuming the time record of, for instance, free surface elevation or wave-induced load on a structure can be approximated by a Stokes-like harmonic series in both frequency and wave steepness, then the higher-order nonlinear contributions to the time record can be separated by using a so-called 'phase-inversion' method. This method requires two tests (either experimental or numerical) using two incident wave trains with identical component amplitudes and frequencies but phases shifted by $\pi$. The underlying assumptions of this method are twofold: the existence of a generalised Stokes-type harmonic series expansion in both frequency and wave steepness, and the validity of Stokes's perturbation expansion up to the target order. This method has been applied to study wave-body interactions in uniform water depth (Zang *et al.* 2006, 2010; Fitzgerald *et al.* 2014) and shoaling waves on variable bottom profiles (Borthwick *et al.* 2006; Zheng *et al.* 2020).

The phase-inversion method is however limited by its capacity in distinguishing $n$-th and $(n+2)$-th order harmonics in a wave group. Especially at higher orders, the overlap between them could occur over a range of frequencies, and it is difficult to separate them accurately with digital filters. In this study, the harmonic separation is achieved with a generalised phase-inversion method recently introduced by Fitzgerald *et al.* (2014), using four phase shifts. The linear primary component and the first three super-harmonics (up to fourth order) can be isolated with linear combinations of four time-histories. The method is here applied to the numerical simulations (as experimental time series are available for a single set of phases). These time-histories come from four whispers3D simulations with the incident signals having the same amplitudes and frequencies but shifted phases, namely 0, $\pi/2$, $\pi$, and $3\pi/2$. The linear combinations of time-histories and separated harmonics are as follows:

$$\eta_{1st} = \left(\eta_0 - \eta^H_{\pi/2} - \eta_\pi + \eta^H_{3\pi/2}\right)/4 = \eta^{(1,1)} + \eta^{(3,1)} + \text{h.o.t.}, \tag{2.12}$$

$$\eta_{2nd} = \left(\eta_0 - \eta_{\pi/2} + \eta_\pi - \eta_{3\pi/2}\right)/4 = \eta^{(2,2)} + \eta^{(4,2)} + \text{h.o.t.}, \tag{2.13}$$

$$\eta_{3rd} = \left(\eta_0 + \eta^H_{\pi/2} - \eta_\pi - \eta^H_{3\pi/2}\right)/4 = \eta^{(3,3)} + \text{h.o.t.}, \tag{2.14}$$

$$\eta_{4th} = \left(\eta_0 + \eta_{\pi/2} + \eta_\pi + \eta_{3\pi/2}\right)/4 = \eta^{(2,0)} + \eta^{(4,4)} + \text{h.o.t.}, \tag{2.15}$$

where the subscripts 0, $\pi/2$, $\pi$, $3\pi/2$ denote the applied phase shift, the superscript $H$ denotes harmonic conjugate of the signal computed via Hilbert transform. For the separated harmonic components $\eta^{(m,n)}$ on the right-hand-side, the first index $m$ in the superscript denotes the power in amplitude, and the second index $n$ the order of harmonic. The higher-order terms with fifth- and higher-order in amplitudes are omitted and represented by 'h.o.t.'. Note that in (2.15) both the fourth-order harmonic $\eta^{(4,4)}$ and second-order difference harmonic $\eta^{(2,0)}$ appear. As the overlap between these two components is very limited, a simple low-pass filter can be applied to separate them.

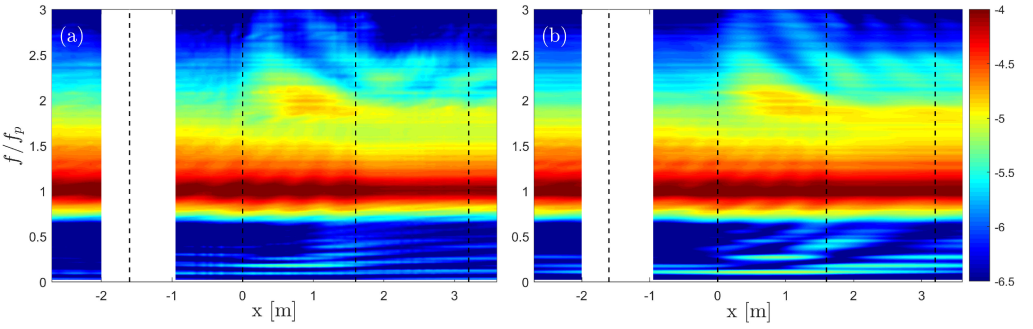



FIGURE 5. Colour maps showing the spatial evolution of variance density spectrum of the free surface elevation of Run 3 calculated from: (*a*) measurements and (*b*) simulation results. The vertical dashed lines indicate the limits of the sloping bottom areas, located at $x = -1.6$ m, 0 m, 1.6 m, and 3.2 m.

## 3. Comparison of simulations and experiments for Run 3 and analysis of wave transformation processes

In this section, a comprehensive comparison between the simulations and measurements of R3 is presented based on the analysis approaches presented in §2.4 (and appendix A) and §2.5. From the simulation results, we extract the same set of data (time-series of $\eta$ and $u(z_0)$) as recorded during the R3 experiment. Moreover, extra information was gathered, including the vertical velocity and the evolution of phase-shifted incident wave trains. In addition to the comparison of free surface elevation in figure 4, more pieces of evidence are needed to illustrate the capacity of the model to capture the dynamics of waves as they propagate along the wave flume. We also aim at better assessing the non-equilibrium dynamics due to the depth transitions.

### 3.1. *Spatial evolution of wave spectrum*

The spatial evolution of measured and simulated wave spectra is shown in figure 5. The area with no measurement between probes 7 ($x = -2$ m) and 8 ($x = -0.95$ m) is intentionally left blank. It can be seen that the measured spectrum in figure 5(a) and the simulated one in figure 5(b) are in good agreement. Both show clearly the enhancement of second-order harmonics in the frequency range $[1.5f_p, 2.5f_p]$ over the shallower region. The energy level of the spectral peak at $f_p$ in the measured spectrum is gradually attenuated in space, whereas this level is more or less unchanged in the simulated spectrum. This is speculated to be a consequence of the dissipation which is not considered in our simulation. The dissipation is more effective in the frequency range near the spectral peak than in the high-frequency range. In the LF range $[0, 0.5f_p]$ of both simulated and measured spectra, some long-waves appear, especially after the up-slope area. The long-waves are of slightly higher energy in the simulation as shown in figure 5(b). As discussed in §2.3, the long-waves observed in both panels (a) and (b) of figure 5 are considered to originate from nonlinear wave-wave interactions. It is therefore considered the slight overestimation of the LF energy in figure 5(b) results from stronger nonlinear interaction due to a more energetic spectral peak in the simulation after the up-slope area.

In figure 6, a more detailed comparison of the spectra measured at eight positions is shown to demonstrate the spectral evolution along the wave flume. Figure 6(a) shows the wave train propagates over the deeper region with very limited changes in the main part of the spectrum ($0.5f_p < f < 3f_p$), indicating the nonlinear wave-wave interactions

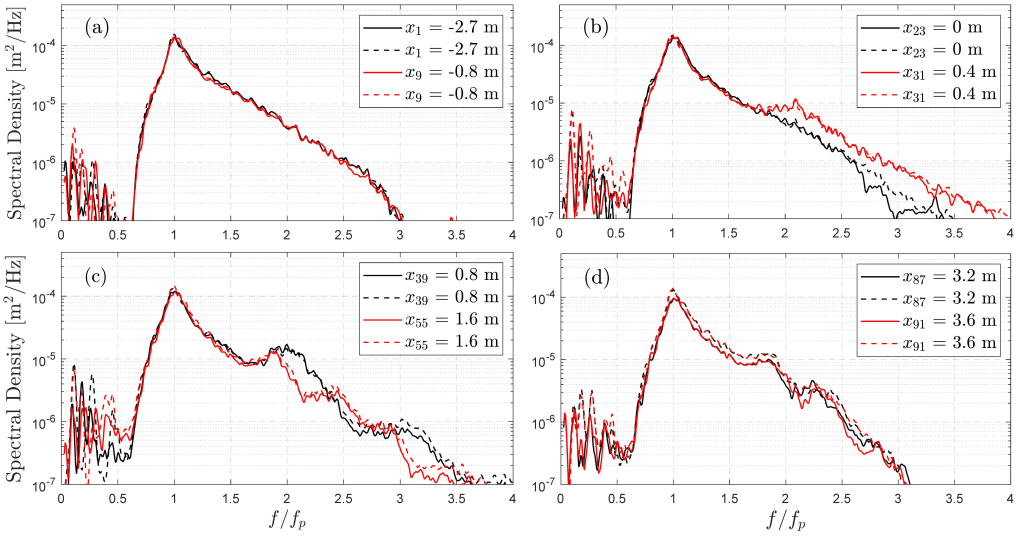



FIGURE 6. Comparison of variance density spectra of surface elevation in different areas: (*a*) the deeper region till the toe of the up-slope; (*b*) the beginning of the shallower region; (*c*) the end of the shallower region; (*d*) deeper region after de-shoaling. In all the panels, the solid lines represent measurements, and dashed lines are simulation results.

are weak in this range. As the wave train propagates in the shallower region, the waves with frequencies higher than $2f_p$ receive energy in a short distance (figure 6(b)). In figure 6(c), at half-length of the shallower region ($x = 0.8$ m), secondary spectral peaks around $2f_p$ and $3f_p$ manifest. As the wave train approaches the end of the shallower region (from probe 39 to 55), the secondary peaks around $2f_p$ and $3f_p$ are shifted toward lower frequencies. In figure 6(d), the spectrum measured at probe 91 ($x = 3.6$ m) has some similarities with the spectrum measured at probe 1 ($x = -2.7$ m), but the secondary peaks close to $2f_p$ and $3f_p$ do not completely vanish. It indicates the spectral changes resulting from a shoaling area are not fully reversible by setting a symmetrical de-shoaling area due to nonlinear effects. The predictions of whispers3D are seen to be very accurate over a wide frequency range for all spectra shown in figure 6.

### 3.2. *Evolution of non-dimensional parameters*

In figure 7, the spatial evolution of twelve non-dimensional parameters is shown in eight panels. For all these parameters, the agreement between the experiment and the simulation is excellent. In figure 7(a), the spatial evolution of two normalised significant wave heights corresponding to the components in frequency range $[0, 0.5f_p]$ (LF waves) and $[0.5f_p, 0.5f_s]$ (short waves) are shown. For the short-wave $H_{m_0}$, small spatial oscillations over the shoal crest can be observed in both experiment and simulation. In the experiment, the $H_{m_0}$ of short waves is attenuated in the shallower flat region (dark grey zone) but almost holds as constants at other locations. The small decrease of $H_{m_0}$ is attributed to the dissipation in the experiment. It is evident that the dissipation is related to the relative water depth, so we speculate that the dissipation in the experiment was mainly induced by friction on the bottom and side-walls. The $H_{m_0}$ for LF waves keeps its low level over all the domain. In figure 7(b), the similar pattern of oscillation of the steepness parameter in the shallower flat region as for $H_{m_0}$ is observed. The increase of the steepness parameter over the up-slope is more pronounced than that of $H_{m_0}$, since the local peak wavelength is reduced due to shoaling.

In figure 7(c), the evolution of the skewness of the free surface elevation $\lambda_3(\eta)$ and the horizontal velocity $\lambda_3(u(z_0))$ show similar increasing and decreasing trends over the domain. Their maximum and minimum values are achieved roughly at the same positions, both located shortly after the change of bottom gradient (maximum at $x \approx 0.6$ m, and minimum at $x \approx 2.3$ m). The skewness indicates the asymmetry of the probability distribution of the considered variable. For $\eta$, a positive skewness indicates waves with sharper crests and flatter troughs, and vice-versa for negative values. According to $\lambda_3(\eta)$, the wave profile is nearly symmetric in the first deeper region and becomes asymmetric with positive skewness over the shallower region. As the wave propagate over the down-slope area, the asymmetry of the wave profile is rapidly inverted. The evolution is similar for the profile of $\lambda_3(u(z_0))$.

In figure 7(d), the values of $\lambda_4(\eta)$ in both experiment and simulation are slightly larger than 3 before the bar. Then, they rapidly increase in the area close to the end of the up-slope, achieving their maxima at the same position as for the skewness. The length of latency is found to be about half of the peak wavelength in the shallower region. Then, $\lambda_4(\eta)$ decreases mildly in a larger area, and eventually goes back to 3 around the end of the domain. No particular change of $\lambda_4(\eta)$ is observed in the de-shoaling area. The evolution trend of $\lambda_4(\eta)$ is well captured by the numerical model, though the maximum value of $\lambda_4(\eta)$ is slightly underestimated by 6%. As was observed in TRJR20, $\lambda_4(u(z_0))$ exhibits a very different behaviour: it does not show any noticeable enhancement over the up-slope area nor over the bar crest, but reaches its maximum value after a short distance in the de-shoaling area. Such behaviour of $\lambda_4(u(z_0))$ is well simulated, including its maximum value.

In figure 7(e), the evolution of the asymmetry parameter is shown. Positive values indicate that, in general, waves are leaning toward the wave-propagation direction, whereas, negative values indicate waves are leaning to the opposite direction. The evolution of asymmetry parameter indicates that the incident waves are almost symmetrical in the horizontal direction for $x < -1$ m. As waves propagate over the bar, the general wave profile leans backward first, and then forward. The most backward-leaning wave profile is achieved in the shallower flat region, and the most forward-leaning profile in the de-shoaling area. We note the largest asymmetry of the sea-state in horizontal direction is achieved before $\lambda_3(\eta)$ takes its maximum and minimum values. This implies the deformations of wave shape in horizontal and vertical directions are largely independent.

Figures 7(f) and 7(g) show that $Q_p$ and $\hat{f}_p$ evolve in an oscillatory manner until the end of the shallower region. After that, the changes of these two parameters are very limited. The evolution of $Q_p$ is remarkably well simulated (figure 7(f)). For $\hat{f}_p$ in figure 7(g), the agreement between the experiment and simulation is also good. The peak frequency is only underestimated, by a few percent at most, in the simulation. By and large, the spectral changes in terms of the spectral width and peak frequency are quite limited.

In figure 7(h), the spatial evolution of the two forms of the B–F index (A 5) and (A 12) is shown in logarithmic scale. In the present case, the threshold $k_p h = 1.363$ for modulation instability is achieved at $x = -0.95$ m and 2.55 m. At these two positions, two forms of the B–F index take 0 because the coefficient $\sqrt{|\beta|/\alpha} = 0$ at this threshold relative water depth (see the expressions of $\alpha$ and $\beta$ in (A 8) and (A 9)). Between these abscissas, waves are expected to be modulationally stable, both $\mathrm{BFI}_{S06}$ and $B_s$ no longer indicate the significance of modulation instability but only characterise the relative importance of nonlinearity and dispersion. Both formulations show significant variations over the up- and down-slopes with similar spatial profiles. The variations of $\mathrm{BFI}_{S06}$ and $B_s$ in the modulationally stable area are large compared to those in the unstable area. Such a significant difference is also due to the property of the coefficient $\sqrt{|\beta|/\alpha}$. It monotonically

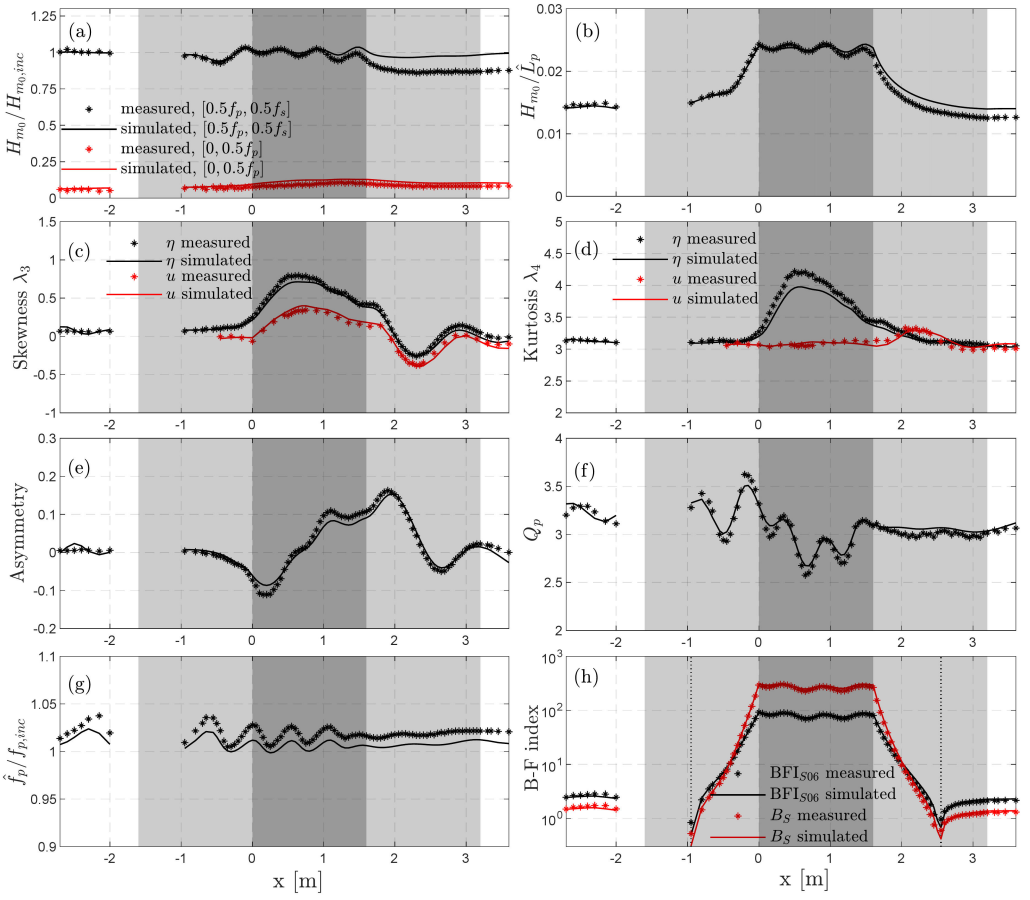



FIGURE 7. Spatial evolution of non-dimensional wave parameters in measurements (∗) and in simulations (solid lines) of R3. The light grey zones indicate the sloping areas and the dark grey zone indicates the shallower flat region. In panel (h), the vertical dash lines denote the positions where the threshold $k_p h = 1.363$ for modulational instability is achieved.

increases from 0 to 1 for $k_p h \geqslant 1.363$, but increases exponentially as $k_p h$ decreases from 1.363 to 0. The magnitude of $B_s$ is higher than that of $\mathrm{BFI}_{S06}$ over the shallower region, due to the correction of the wave-induced mean flow. In line with the evolution of $H_{m_0}$ and steepness parameter, the evolution trend changes right after the transition points of bottom gradient for B–F index. It means the change of nonlinearity due to depth variations is more significant than that of the dispersion, and the changes stop immediately when waves enter flat bottom regions.

### 3.3. *Bispectrum and bicoherence*

Bispectral analysis of $\eta$ time series allows gaining insight on nonlinear wave coupling between modes. In figures 8 and 9, we show the bicoherence for the relative strength of nonlinear coupling and imaginary part of the bispectrum for the energy transfer direction, in the area from 0.25 m to 1.3 m (over the shallower region). In this area, the skewness and kurtosis vary significantly, with their maximum values achieved at $x \approx 0.6$ m. It indicates the most active nonlinear interaction takes place in this area. Each panel contains the bispectrum from measurements in the lower right triangle and

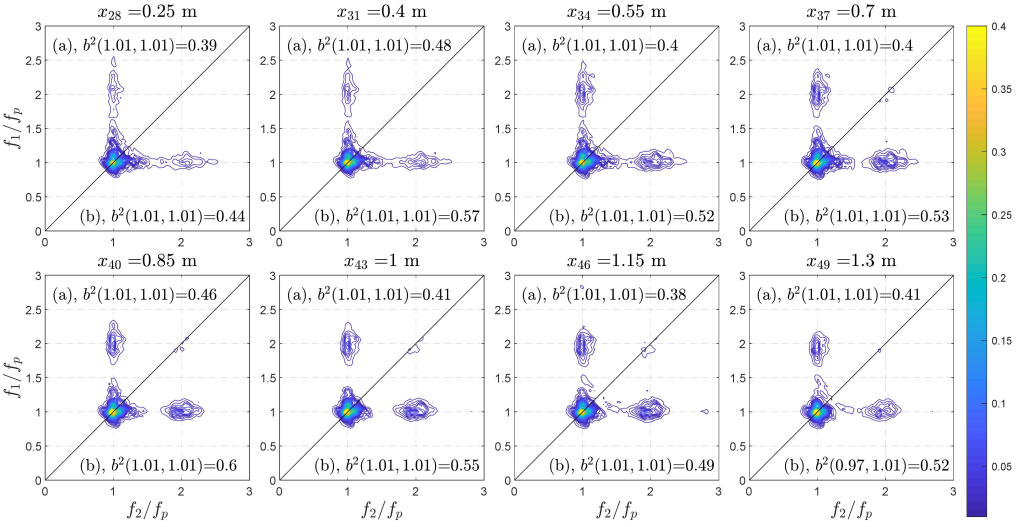



FIGURE 8. Contours of bicoherence over the shallower region at eight probe positions between $x = 0.25$ m (probe 28) and $x = 1.3$ m (probe 49), in ($a$) simulated results; ($b$) measurements. The probe numbers and positions are indicated on each panel, together with the corresponding maximum bicoherence values.

the bispectrum from simulation in the upper left triangle (so that the agreement between them can be estimated from the symmetry about the line $f_1 = f_2$).

From the evolution of bicoherence $b^2$ shown in figure 8, we note the strongest interaction always takes place in the region near the spectral peak. The strongest coupling achieved at $b^2(1.01f_p, 1.01f_p)$ reflects intense energy transfer among $f_1 = 1.01f_p$, $f_2 = 1.01f_p$, and $f_1 + f_2 = 2.02f_p$. This interaction corresponds to the development of the second harmonics around $2f_p$ in the spectrum. A less strong but clearly visible interaction takes place around $b^2(2f_p, f_p)$, which becomes increasingly significant as waves propagate from $x = 0.25$ m to 1.3 m. It corresponds to the development of the third harmonics around $3f_p$. More generally, we notice the non-zero bicoherence in the range between $b^2(f_p, f_p)$ and $b^2(2f_p, f_p)$ from probe 28 to 34, which indicates that the harmonics with frequencies $2f_p \leqslant f \leqslant 3f_p$ are involved in the interactions. This is in agreement with the observations in figure 6(b) where a clear increase is noticed for the whole tail of the spectrum above $2f_p$ at probe 31. After some distance, non-zero values of $b^2$ appear only around $b^2(f_p, f_p)$ and $b^2(2f_p, f_p)$ resulting in the formation of second and third harmonics. In the simulation, not only the components of the nonlinear interactions but also the levels of bicoherence are well predicted for the listed probes.

In figure 9, the energy transfer direction can be inferred, by considering the imaginary part of the bispectrum. Positive values indicating sum interactions are represented by colours from green to red. Meanwhile, negative values indicating difference interactions are represented by green to blue. It is clearly seen that the sum interactions first take place over the first half of the shallower flat region (from probe 28 to 34), forming the second harmonics around $2f_p$. Close to the centre of the shallower region, at probes 37 and 40, difference interactions appear around $(f_p, f_p)$, indicating energy transfer from second harmonics $2f_p$ back to $f_p$ mode. In this area, both the sum and difference interactions are present. As waves approach the second half of the shallower region (from probe 43 to 49), difference interactions dominate. Besides, difference interactions are present around $\mathrm{Im}\{B(f_p, 0.25f_p)\}$. It indicates energy transfer from the frequency $1.25f_p$ to $f_p$

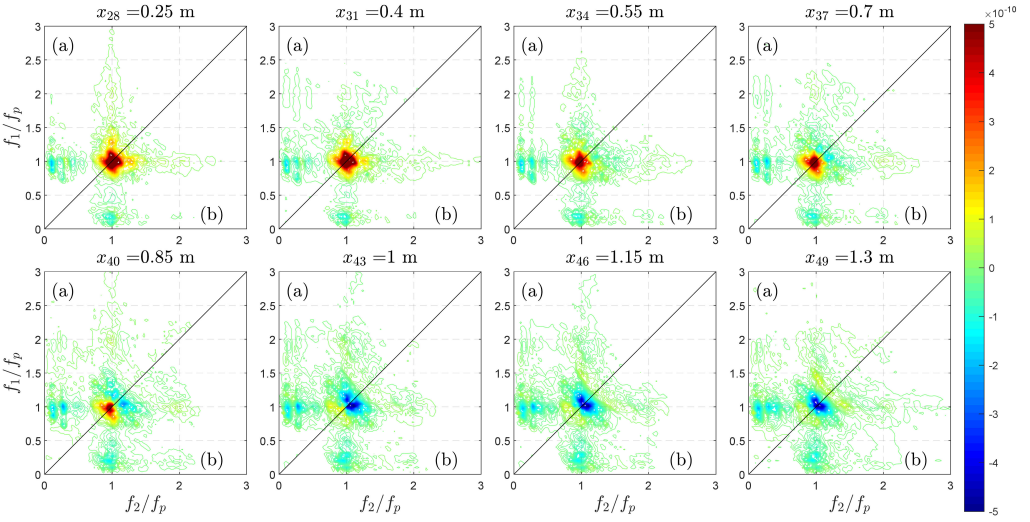



FIGURE 9. Contours of the imaginary part of bispectrum over the shallower region at eight probe positions between $x = 0.25$ m (probe 28) and $x = 1.3$ m (probe 49), in ($a$) simulated results; ($b$) measurements. The probe numbers and positions are indicated above each panel.

and $0.25f_p$, thus the generation/enhancement of LF waves with frequency $0.25f_p$. In general, the agreement between simulation and experiment is very good. Only some small differences can be observed in the LF range, which explain the overestimation of LF energy in the simulated spectrum in figure 5(b).

### 3.4. *Harmonic analysis*

The application of the generalised phase-inversion method outlined by Fitzgerald *et al.* (2014) requires moderate nonlinearity of the sea-state, in order to adopt a Stokes-type harmonic series to represent the time series of $\eta$. As wave nonlinearity is significantly enhanced due to shoaling, attention should be paid to the applicability of this approach in the current case. To evaluate the applicability of the harmonic separation technique in the present case, the sea-state is represented by the so-called first-, second-, and third-order harmonics. These characteristic waves are of frequencies $f_p$, $2f_p$, and $3f_p$ respectively, and their representative wave heights are computed in the same way as for the significant wave height but over different frequency ranges, namely $[0.5f_p, 1.5f_p]$, $[1.5f_p, 2.5f_p]$, and $[2.5f_p, 3.5f_p]$. The representative frequencies and wave heights are computed locally and averaged over the areas with constant depth $h_1$ and $h_2$. In figure 10, the representative harmonics are placed in the diagram of Le Méhauté (1976). It is seen the first three harmonics fall in the range of validity of Stokes second-order theory in both flat regions: the harmonic separation method is thus applicable.

After running three additional simulations with $\pi/2$, $\pi$ and $3\pi/2$ phase shifts for the incident wave train, the contributions of harmonics at different orders $\eta_{1st}$, $\eta_{2nd}$, $\eta_{3rd}$, $\eta_{4th}$ to the original time record of $\eta$ can be evaluated from equations (2.12–2.15). The spatial evolution of their spectra is shown in figure 11. It can be seen that the different harmonics have been successfully extracted. The spectrum of the primary components (panel (a)) evolves with nearly no modulation over the domain. Panel (b) indicates the increase of energy around $2f_p$ is mainly due to second-order sum interactions. In panel (c), the third harmonic is seen to be weak except over the bar crest. In panel (d) showing $\eta_{4th}$, two components $\eta^{(4,4)}$ and $\eta^{(2,0)}$ should be present according to (2.15). However the

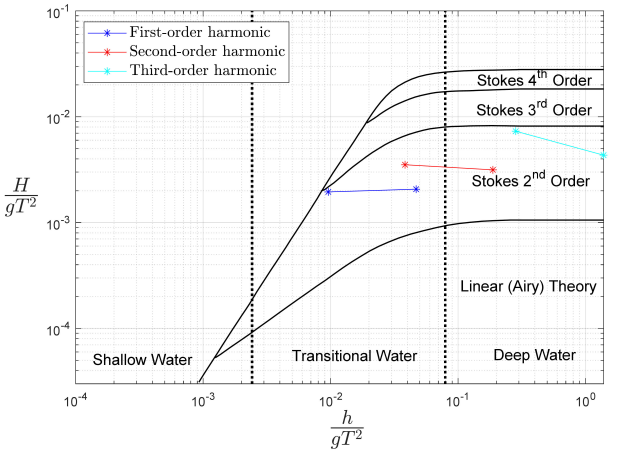



FIGURE 10. Le Méhauté's diagram (Le Méhauté 1976), with the first three representative harmonics of the irregular wave train of R3 added.

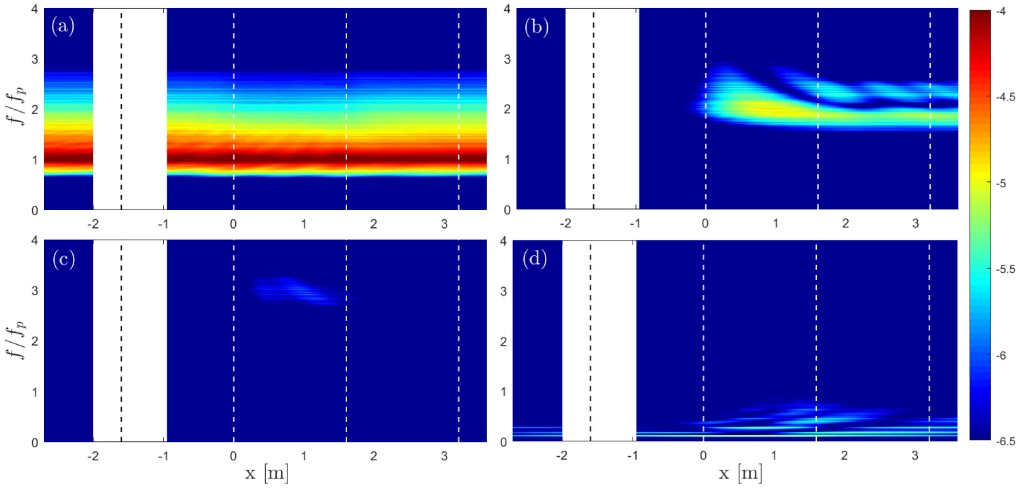



FIGURE 11. Spatial-spectral evolution of extracted harmonics at different orders (in logarithmic scale): $(a)$ the first-order component $\eta_{1st}$, $(b)$ the second-order component $\eta_{2nd}$, $(c)$ the third-order component $\eta_{3rd}$ and $(d)$ the fourth-order component $\eta_{4th}$. The vertical dashed lines indicate the limits of the sloping bottom areas, located at $x = -1.6$ m, 0 m, 1.6 m, and 3.2 m.

fourth harmonic $\eta^{(4,4)}$ is weaker than the lower bound of the current colour scale, with negligible contribution here. Therefore $\eta_{4th} \approx \eta^{(2,0)}$, showing the role of second-order difference interactions in driving the energy increase of LF waves.

We note that Zheng *et al.* (2020) applied this technique using the phase-inversion approach (i.e. with two time series $\eta$ and $\eta_\pi$), resulting in the separation of $(\eta_{1st} + \eta_{3rd})$ and $(\eta_{2nd} + \eta_{4th})$, denoted as $\eta_{odd}$ and $\eta_{even}$ respectively. Clearly, the two separated components $\eta_{odd}$ and $\eta_{even}$ would be subject to some overlap. In the present work, the generalised (four-phase) phase-inversion method permits to isolate the first four harmonics with good quality.

Basing on this decomposition, we analyse the contribution of the four harmonics to the changes of skewness and kurtosis by considering cumulative summations of the separated signals (figure 12). In panel (a), the skewness of the primary component is nearly 0.

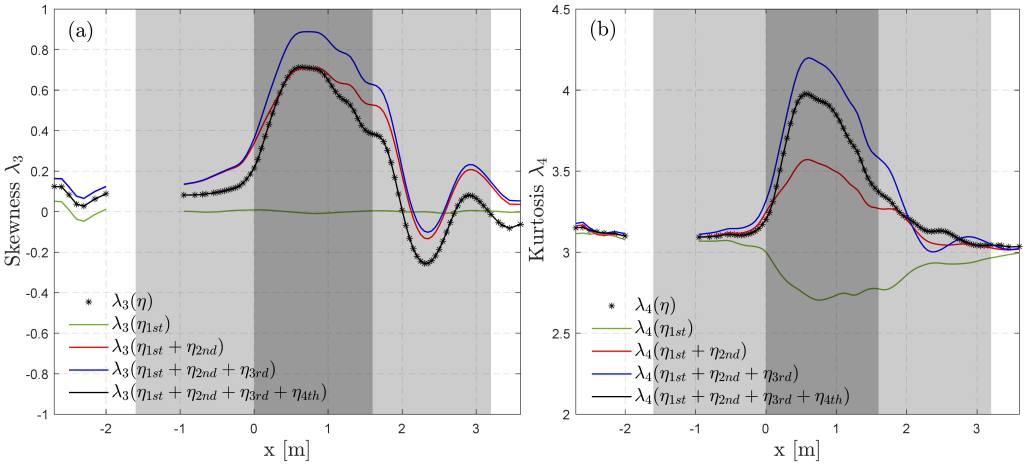



FIGURE 12. Spatial evolution of ($a$) skewness and ($b$) kurtosis of the time series of $\eta$ obtained from the simulation of R3-bar case without phase shift, and different combinations of separated time series (see legend).

By adding the contribution due to second-order sum interaction, $\lambda_3(\eta_{1st} + \eta_{2nd})$ is significantly enhanced, showing very similar variations in space as $\lambda_3(\eta)$. The second harmonic thus dominates the changes of skewness over the entire domain. Although $\eta_{3rd}$ has little contribution to the spectrum, see figure 11(c), it affects skewness evolution in a non-negligible way. Furthermore, the effects of $\eta_{3rd}$ appear only in the area where the sea-state is out-of-equilibrium, namely starting shortly after the up-slope and ending shortly after the shallower flat region. We note $\lambda_3(\eta_{1st} + \eta_{2nd} + \eta_{3rd})$ is larger than $\lambda_3(\eta)$, indicating that the LF components due to second-order difference interactions are responsible of a decrease of skewness.

In figure 12(b), it is observed that the kurtosis of the primary component becomes lower than 3 as water depth decreases. The second harmonic component, $\eta_{2nd}$, affects the kurtosis over the entire domain, with an evident enhancement over the bar crest. The inclusion of $\eta_{3rd}$ significantly enhances the kurtosis over the same area as for skewness. Again, the contribution of bound LF waves $\eta_{4th}$ results in a decrease of kurtosis. Based on these observations, it is anticipated that the changes of skewness and kurtosis due to shoaling are related to both second- and third-order nonlinear interactions in the current case, and the non-equilibrium dynamics is associated with third-order effects, resulting in significant enhancement of kurtosis.

### 3.5. *Statistical distributions*

In figure 13, the PDFs of $\eta$ time-series at 6 probes over the bar are shown, with the Gaussian PDF superimposed as a reference. The measured and simulated PDFs show excellent agreement for all the probes shown. In the experiment, the sea-state remains quasi-Gaussian until the end of the up-slope (probe 23). Over the bar crest (from probe 23 to 55), strong deviations from Gaussianity manifest. The positive tail of the distribution is shifted toward higher values of $\eta/\sqrt{m_0}$ indicating that the highest wave crests are noticeably larger in comparison with the Gaussian prediction. Meanwhile, the negative tail is shifted toward lower values, indicating the wave troughs are shallower. Such observations are in agreement with the expectation of positive skewness in this area. Among all the positions shown here, the strongest non-Gaussian behaviour takes place close to the middle of the shallower region (probes 35 to 39), at the length of latency.

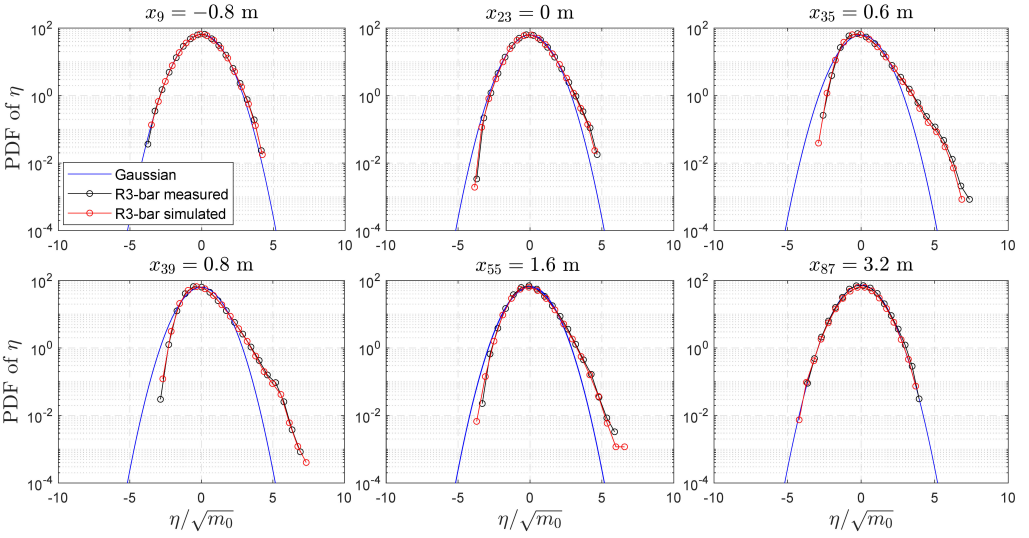



FIGURE 13. Probability density function (PDF) of free surface elevation ($\eta$) at 6 probe positions between $x = -0.8$ m (probe 9) and $x = 3.2$ m (probe 87). The probe numbers and positions are indicated above each panel. The Gaussian distribution is superimposed to highlight the nonlinear characteristics of the sea-state.

At the end of the bar crest (probe 55), the deviation of the empirical PDF from the Gaussian one decreases. This is related to the effects of de-shoaling and the weakening of the non-equilibrium dynamics. This is also in agreement with the indication of bispectral analysis, from which we found energy transfer from second harmonic $2f_p$ back to peak frequency $f_p$, and a decrease of nonlinear interactions. Eventually, at the end of the de-shoaling zone (probe 87), the empirical PDF turns back to Gaussian.

In figure 14, the CCDFs of wave height $H$ are shown at the same positions as in figure 13, with the distribution of Boccotti (2000) superimposed as reference. Again, the agreement between the simulation and measurements is excellent, even in the tail of the distributions. Only few of the largest waves are slightly higher in the simulation at probes 39 and 55. Starting as a quasi-Gaussian process at probes 9, the sea-state undergoes a clear deviation from Gaussianity as waves propagate over the bar crest, with a marked increase of large waves, in particular at probes 35 and 39, and to a lesser extent until the end of this area (probe 55). Over the bar crest, and in particular in the zone $0.5 \text{ m} < x < 1 \text{ m}$, several "freak waves" can be identified basing on the criterion $H > 2H_{m_0}$. The distribution of Boccotti (2000) predicts that the occurrence probability of waves with $H > 2H_{m_0}$ is lower than 0.01% (the lower limit of the y-axis in figure 14). In agreement with the increase of $\lambda_4(\eta)$ discussed previously (see figure 7(d) or 12(b)), these wave height distributions clearly demonstrate the increase of the occurrence probability of freak waves due to the water depth transition. At the end of the de-shoaling area (probe 87), where the PDF of $\eta$ is very close to Gaussian in figure 13, the empirical CCDF of $H$ is lower than the theoretical prediction in the high-wave range. We note the CCDF of $H$ at probe 87 is rather close to the distribution observed before the bar crest (probe 9), with a reduction of the occurrence probability of large waves. This is again considered to be an effect of the de-shoaling process.

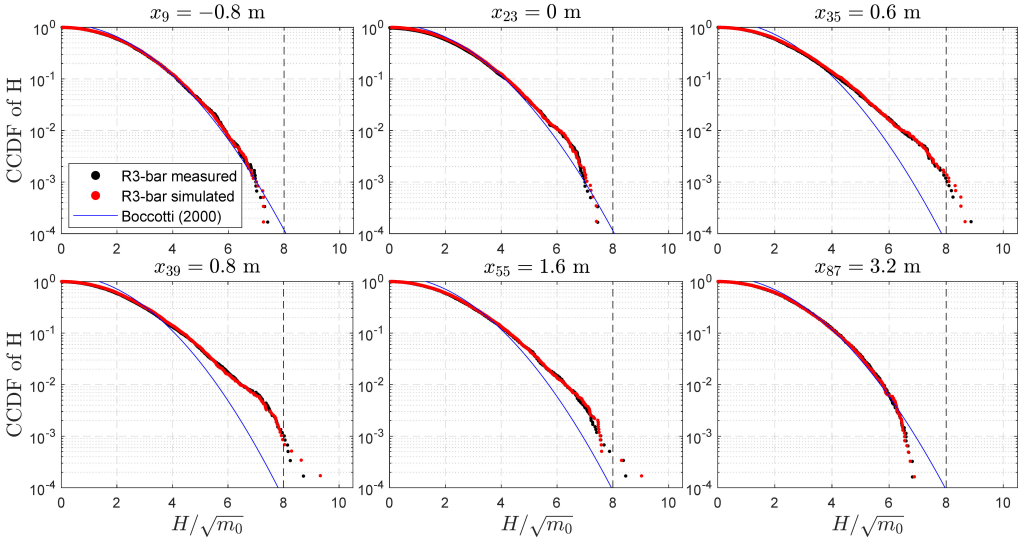



FIGURE 14. Complementary cumulative distribution function (CCDF) of wave height ($H$) at 6 probe positions between $x = -0.8$ m (probe 9) and $x = 3.2$ m (probe 87). The probe numbers and positions are indicated above each panel. The vertical dashed line in each panel represents the commonly adopted threshold for freak waves: $H = 2H_{m_0}$.

### 3.6. *Statistics of velocity and acceleration*

In R3 experiment, the horizontal velocity at $z_0 = -0.048$ m has been measured at 37 positions, and studied statistically in TRJR20. In §3.2 we have shown the skewness and kurtosis of $u(z_0)$ simulated with whispers3D are in excellent agreement with the measurements (see figure 7(c-d)). Here, using additional model results, we present a more complete statistical analysis of the kinematic properties, namely the vertical velocity and accelerations in both directions. The local (Eulerian) horizontal and vertical accelerations, denoted as $u_t(z_0)$ and $w_t(z_0)$ respectively, are evaluated as time derivatives of $u(z_0)$ and $w(z_0)$. The computation of derivatives is made with a five-point centred finite difference scheme. In the following, we analyse the spatial evolution of the skewness and kurtosis of 5 variables: $\eta, u(z_0), w(z_0), u_t(z_0), w_t(z_0)$.

In figure 15(a), the evolution of skewness of the 5 kinematic variables is plotted. Two groups of variables can be identified, showing two different spatial evolution patterns. First, we note $\lambda_3(w(z_0))$ and $\lambda_3(u_t(z_0))$ evolve very closely over the whole domain. They both reach two local maximum and one local minimum values, at almost the same positions for both variables (first maximum at $x \approx 0.2$ m, minimum at $x \approx 1.9$ m, second maximum at $x \approx 2.6$ m). In addition, it is noticed that the profile of the asymmetry parameter in figure 7(c) is similar to that of $\lambda_3(w(z_0))$ and $\lambda_3(u_t(z_0))$, despite an opposite sign. In the second group, the spatial profiles of $\lambda_3(\eta)$, $\lambda_3(-w_t(z_0))$ and $\lambda_3(u(z_0))$ present a lot of similarities, though with different magnitudes. The local maximum and minimum values of skewness of these 3 variables are located downstream compared to the ones of $w(z_0)$ and $u_t(z_0)$. The skewness of $w_t(z_0)$ shows the most pronounced variation, with its global maximum achieved around $x = 0.45$ m. The skewness of $u(z_0)$ shows a lower minimum value in the middle of the down-slope area (around $x = 2.3$ m). The spatial profiles of the skewness of these 5 variables and the asymmetry parameter indicate that the adaptation of the sea-state due to depth variations has different impacts on kinematic properties, among which two dominant typical evolution patterns can be identified.

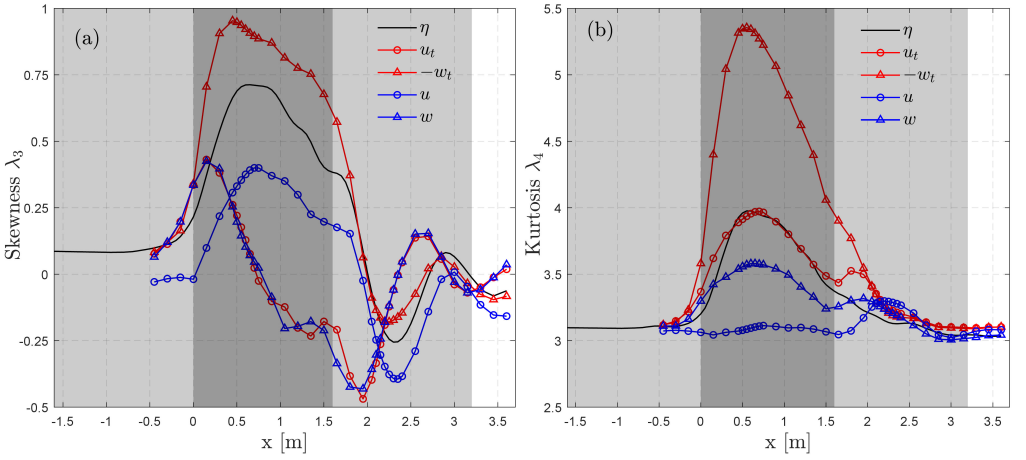



FIGURE 15. Spatial evolution of (a) skewness and (b) kurtosis of five variables obtained from the simulation of R3-bar case: free surface elevation $\eta$, horizontal and vertical velocities $u$, $w$, horizontal and vertical accelerations $u_t$, $w_t$. The velocities and accelerations are computed at the same elevation $z_0 = -0.048$ m.

It is known from linear theory that $\eta, u$ and $-w_t$ are of the same phase in a linear superposition of progressive harmonic components, while $w$ and $u_t$ are also in phase, but with a phase shift of $\pi/2$ with respect to the variables of the former group. In the nonlinear case, such an expectation is not guaranteed *a priori*. The observations in figures 15(a) indicate that the phase relations among the five variables are somewhat preserved in the present case.

Figure 15(b) shows the kurtosis evolution of the same variables. As was observed in TRJR20, $\lambda_4(u(z_0))$ shows no sign of enhancement over the up-slope or the bar crest, whereas a local maximum is achieved in the down-slope area. This trend is successfully captured in the simulation. However, model results show that $\lambda_4(w(z_0))$, $\lambda_4(u_t(z_0))$ and $\lambda_4(-w_t(z_0))$ (not discussed in TRJR20) are noticeably enhanced over the shallower region, with their maximum values achieved at the same position (about $x = 0.6$ m, corresponding to the length of latency) as for $\lambda_4(\eta)$. Regarding the variables $u_t(z_0)$ and $w(z_0)$, we note that their kurtosis profiles are very similar, as was observed for their skewness profiles in figure 15(a). $\lambda_4(-w_t(z_0))$ shows the most significant enhancement over the bar crest with only one maximum in the domain, as for $\lambda_4(\eta)$. Our results supplement the observations made on $\lambda_4(u(z_0))$ in TRJR20, showing that significant changes of kurtosis of other kinematic properties, namely $w(z_0)$, $u_t(z_0)$ and $-w_t(z_0)$, take place due to depth variations. Furthermore, the kurtosis profiles of these 3 variables are markedly different from the one of $u(z_0)$. All three show a significant increase of kurtosis over the bar crest (implying an increased occurrence probability of their maximum values), in line with the increase of $\lambda_4(\eta)$ in this area.

## 4. Effects of finite length of the bar crest and de-shoaling

### 4.1. *Objectives and outline of the simulation with a step-like profile*

In §3, an extensive analysis of the effects induced by wave shoaling in the up-slope area has been performed, together with the effects of the down-slope (de-shoaling). At the up-slope transition, the out-of-equilibrium dynamics of the wave train is associated with the spectral settling from the deeper-water equilibrium state (in depth $h_1$) to the shallow-

water equilibrium (in depth $h_2$), and this process takes place over a certain distance after the start of the shallower region. However, this shallower water area is of relatively short length in the R3-bar setup. One may wonder whether the out-of-equilibrium dynamics due to up-slope transition has been fully developed in the shallower region and what is the contribution of the de-shoaling process. The sea-state could enter the de-shoaling area before having reached a new shallow-water equilibrium, it is therefore difficult to conclude which effects govern the sea-state dynamics after the shallower region.

In order to isolate the effects of the two slopes and to better assess the characteristic distance of non-equilibrium dynamics due to the shoaling process, an additional simulation without the de-shoaling area has been conducted with a modified bathymetry profile (R3-step setup in figure 2(b)). The simulation of the new case is conducted with the same numerical parameters as for R3-bar case. In this section, we show the results of this new R3-step case, and compare them with those of R3-bar case. We focus on the spatial evolution of the variance density spectrum (§4.2), non-dimensional parameters (§4.3) and the statistics of the kinematic variables (§4.4).

### 4.2. *Spatial evolution of wave spectrum*

In figure 16, the spectral evolution in space shows the wave spectra of the two setups exhibit very similar patterns in the area where the bottom profiles are identical ($x < 1.6$ m). After $x = 1.6$ m, the differences in the spectra manifest mainly for two frequency ranges: $f > 1.5f_p$ and $f < 0.5f_p$. In R3-step case, more energy is transferred to components in these two ranges, which is clearly the consequence of stronger nonlinear interactions in the extended shallower region. In figure 16(b) for R3-step case, a second energetic peak around $2f_p$ appears after $x \approx 2.5$ m and lasts until the end of the domain.

In the area from $x = 1.6$ m to 3.6 m, there is a particular spatial evolution of the spectrum for $f > 1.6f_p$, quite different from R3-bar case. It is believed this particular spatial structure in the high-frequency range is due to the simultaneous presence of free and bound components with frequencies being higher harmonics of frequencies close to the spectral peak (typically in the range $[0.8f_p, 1.5f_p]$). This situation is typically encountered when waves propagate over a submerged bar or shoal (Beji & Battjes 1993) or when waves are generated using a wave shape that does not correspond to the stable form of progressive nonlinear waves for the considered depth (Chapalain *et al.* 1992). As it is well-known, if free and bound components at a higher harmonic $Nf$, with $N = 2, 3, ...$, of the primary frequency $f$ coexist in constant depth, a beating or spatial modulation of the amplitude will manifest. This effect is most apparent here for the second harmonics ($N = 2$) of primary frequencies $f \in [0.8f_p, 1.5f_p]$. The beat length of second harmonics, defined as the distance between two successive maximum values of the spectral amplitude, can be estimated following Massel (1983):

$$L_{beat}(2f) = \frac{2\pi}{k(2f) - 2k(f)}, \tag{4.1}$$

where the wave-numbers $k(f)$ and $k(2f)$ are computed from $f$ and $2f$ using the linear dispersion relation (for depth $h_2$). Following this idea, the beating length of second harmonics for $f \in [0.8f_p, 1.5f_p]$ have been computed and superimposed in figure 16(b). The estimation of the beating length for $f \in [0.8f_p, 1.5f_p]$ results in a series of curves in the range $[1.6f_p, 3f_p]$ as second harmonics. The distance between two successive curves at a particular frequency corresponds to the beating length. These curves are in good agreement with the spatial modulations of the spectrum in figure 16(b) for $f > 1.6f_p$.

In the R3-bar case (figure 16(a)), this effect is less pronounced due to the variable depth over the down-slope area, but still visible for $f > 2f_p$. It is also noted that for the case of

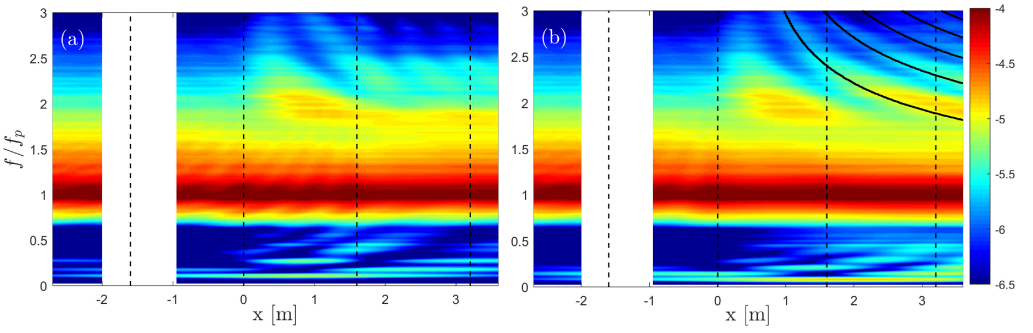



FIGURE 16. Spatial evolution of the variance density spectra in simulations ($a$) with R3-bar setup, and ($b$) with R3-step setup. The vertical dashed lines indicate the limits of the sloping bottom areas in R3-bar setup, located at $x = -1.6$ m, 0 m, 1.6 m, and 3.2 m. The solid black curves in panel ($b$) represent the predicted maximum values of the spectral amplitude, between which the distance in space corresponds to the beating length of the second harmonics of primary frequencies in $[0.8f_p, 1.5f_p]$.

a larger (uniform) depth in (4.1), the beat length would be reduced. This reduction does not appear clearly after the down-slope area in figure 16(a). This is because the area with constant deeper water ($h_1 = 0.53$ m) after $x = 3.2$ m is only 0.4 m long, which is less than the shortest beating length $L_{beat}(3f_p) \approx 0.42$ m in the considered frequency range $[0.8f_p, 1.5f_p]$. However, comparing the spectra of two simulations in the range $x > 1.6$ m and $f/f_p > 2$, some indication of this reduction can be detected in figure 16(a), though the depth is not uniform from $x = 1.6$ m to 3.2 m in the R3-bar case. In summary, the water depth reduction due to the up-slope results in an increase of wave nonlinearity in the shallower area, which manifests in the forms of energy transfer, generation of bound long-waves and increase of the amplitude of the bound super-harmonics of the frequencies near the spectral peak. In addition, as the depth variation is rather abrupt, part of the energy is also transferred to free waves in the same high-frequency range, resulting in the above-described spatial modulation of spectrum magnitude.

In figure 17, the comparison of the spectra in two simulations is shown at four positions after $x = 1.6$ m. At $x = 1.6$ m (figure 17(a)), the main parts of the two spectra are superimposed. As waves propagate in the extended shallower region in R3-step case, differences gradually manifest in figure 17(b-d). In R3-step case, the harmonic peak around $2f_p$ is more pronounced in comparison with R3-bar case, and we notice this peak is gradually shifted from frequencies slightly higher than $2f_p$ to lower frequencies. We also note the spectrum tail in the range $[2.5f_p, 4f_p]$, which is decreased in R3-bar case, is preserved in the R3-step case. This indicates that the de-shoaling process results in a loss of energy of the high-frequency waves. The LF waves receive more energy in R3-step case due to stronger nonlinear interactions in the extended shallower region for $x > 1.6$ m. In R3-bar case, the spectral evolution in figure 17(b-d) is quite limited. It indicates that the spectral adaptation to the shallow-water equilibrium was not fully developed over the 1.6 m long bar crest in R3-bar case, and was balanced by the de-shoaling process.

### 4.3. *Non-dimensional parameters*

Figure 18 compares the spatial profiles of twelve non-dimensional parameters for R3-bar and R3-step cases. In figure 18(a), the small spatial modulations of $H_{m_0}/H_{m_0,inc}$ calculated in the main frequency range $[0.5f_p, 0.5f_s]$ disappear over the shallower region in R3-step case. It indicates that the de-shoaling process can influence the upstream wave field, possibly via the generation of reflected free waves. Similar trends can be found for

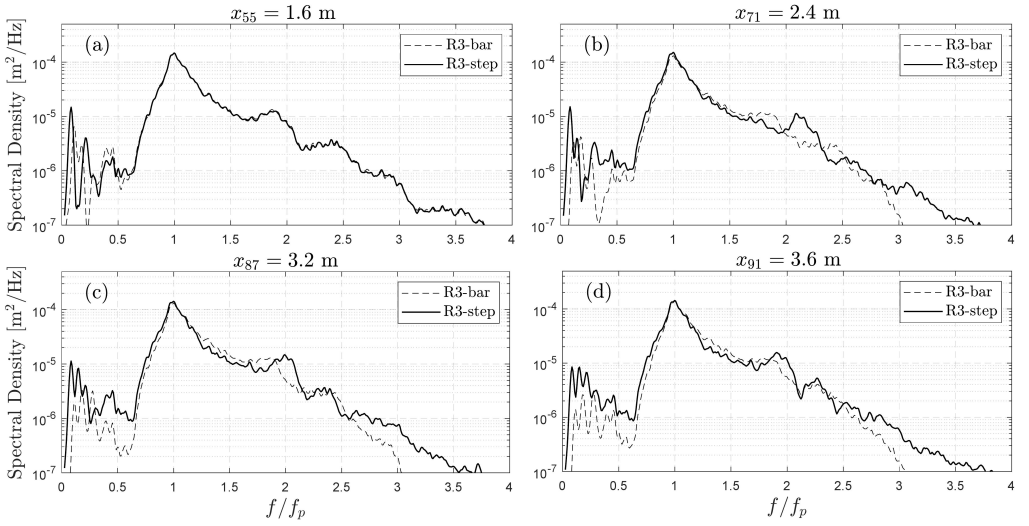



FIGURE 17. Comparison of spectra of the surface elevation at 4 positions from numerical simulations for the R3-step (solid lines) and the R3-bar (dashed lines) cases.

the evolution of steepness parameter, $Q_p$ and $\hat{f}_p/f_p$. In R3-step case, the $H_{m_0}$ of the LF range keeps increasing in the extended shallower region. Due to strong nonlinear interactions in this region, wave energy is continuously transferred toward these sub-harmonic components. In figure 18(b), the decrease of the steepness parameter for $x >$ 1.6 m disappears in R3-step case, because $\hat{L}_p$ remains uniform in the extended shallower region.

In figure 18(c-e), significant discrepancies of skewness, kurtosis and asymmetry parameters from the results of R3-bar case are observed for $x > 1.6$ m. In R3-step case, these parameters are seen to converge toward new constant levels in the extended shallower region, after reaching their maximum/minimum values over the original shallower region. This is an indication that the sea-state is evolving toward a new equilibrium state in the shallower region, since the effects of non-equilibrium dynamics induced by the up-slope gradually decrease in space. In the range $x < 1.6$ m, where both profiles are identical, these statistical parameters are almost superimposed. We thus conclude that the local minimum value of $\lambda_3(\eta)$ and $\lambda_3(u(z_0))$, the local maximum of $\lambda_4(u(z_0))$, and the variations of the asymmetry parameter, observed for $x > 1.6$ m in R3-bar case (see figure 7(c-d)), are caused by de-shoaling effects. This is of interest for interpreting the particular behaviour of $\lambda_4(u(z_0))$ highlighted in figure 7(d): the local maximum of $\lambda_4(u(z_0))$ is not due to the up-slope transition, but to the down-slope one. In R3-step case, $\lambda_4(u(z_0))$ shows nearly no variation over the whole domain, in contrast to $\lambda_4(\eta)$ that experiences strong enhancement in the first part of the shallower region.

Figure 18(f) and 18(g) show the comparison of $Q_p$ and $\hat{f}_p/f_p$, respectively. For these parameters, the differences between the two setups are not restricted to the de-shoaling area but also manifest in the area where the two bottom profiles are identical. The spatial modulations of $Q_p$ and $\hat{f}_p/f_p$ seen in R3-bar case for $x < 1.6$ m become insignificant in R3-step case. As explained above, this indicates that de-shoaling affects not only the wave field in the area after the beginning of the down-slope but also the upstream wave field (reflected waves). Besides this difference, both cases show another modulation of $Q_p$ and $\hat{f}_p/f_p$ before entering the shallower region (i.e. for $x < 0$) attributed to the reflection of incident waves on the up-slope part. In summary, this comparison highlights the fact

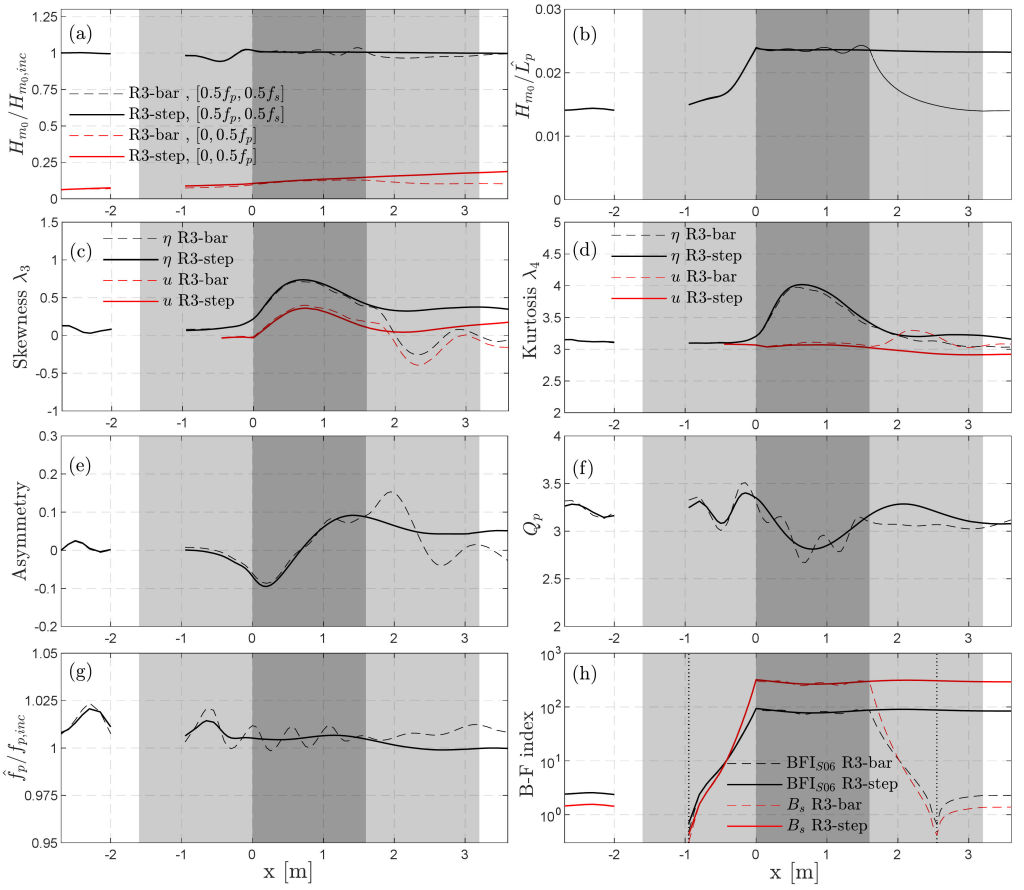



FIGURE 18. Spatial evolution of non-dimensional parameters in simulations of R3 case with de-shoaling area (dashed lines), and without de-shoaling area (solid lines). The light grey zones indicate the sloping areas and the dark grey zone indicates the shallower flat region in the case with the de-shoaling area. In panel (h), the vertical dash lines denote the positions where the threshold $k_p h = 1.363$ for modulational instability is achieved.

that the spatial modulations of $Q_p$ and $\hat{f}_p/f_p$ observed in R3-bar case before $x = 1.6$ m originate from two reflection processes taking place at the up-slope transition (in both cases), and at the down-slope transition (in R3-bar case only).

Figure 18(h) shows the $\mathrm{BFI}_{S06}$ and $B_s$ parameters in the R3-step case are almost superimposed with the ones in R3-bar case for $x < 1.6$ m. However, no decrease after $x = 1.6$ m is seen in R3-step case, due to the extended shallower region.

### 4.4. *Statistics of velocity and acceleration*

Figure 19 compares the spatial profiles of skewness (panel (a)) and kurtosis (panel (b)) of the kinematic properties in the two simulations. In R3-step case, the skewness of all the kinematic properties continue their decreasing or increasing trend over a short distance in the extended shallower region. This is because the non-equilibrium dynamics induced by the up-slope keeps having effects after $x = 1.6$ m. After a short distance in the extended shallower region, the variations of skewness in R3-step case become mild. But it is evident that the steady shallow-water state has not been established yet, even in R3-step case. As an evidence, $\lambda_3(u(z_0))$ keeps its increasing trend until the end of the flume.

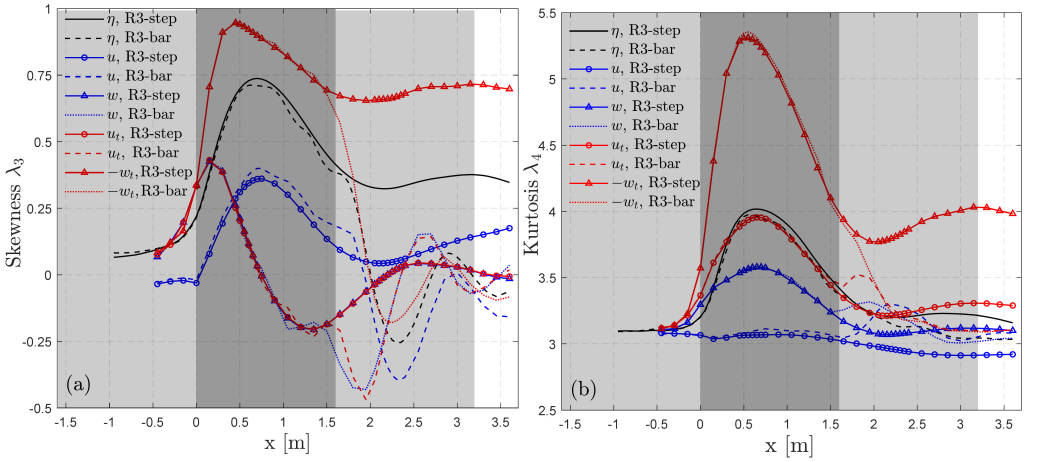



FIGURE 19. Spatial evolution of ($a$) skewness and ($b$) kurtosis of five variables $\eta$, $u(z_0)$, $w(z_0)$, $u_t(z_0)$ and $-w_t(z_0)$ in both R3-bar and R3-step cases.

Based on the observations in Zhang *et al.* (2019) where a long shallower region was used, we anticipate that the mild modulation of skewness in R3-step case would continue over a longer distance without significant changes if the flume was extended. The skewness differences between the two bottom setups correspond to the de-shoaling effects, and it is clear that the de-shoaling process results in opposite effects to the skewness compared to shoaling. The sharp decrease of skewness after $x = 1.6$ m is mainly due to de-shoaling effects (rather than the decrease of up-slope induced non-equilibrium dynamics). It is also noticed that the de-shoaling process slightly influences $\lambda_3(u(z_0))$ and $\lambda_3(\eta)$ before the down-slope area. Regarding skewness, the most sensitive variable to the change of water depth is $w_t$.

In line with the observations for skewness, figure 19(b) shows the kurtosis of the five variables continue their decreasing trend over a short distance in the extended shallower region in R3-step case. This is due to the weakening of non-equilibrium dynamics. The differences of kurtosis between R3-step and R3-bar cases again correspond to the de-shoaling effects. Unlike skewness, both shoaling and de-shoaling processes result in enhancement of kurtosis. Since kurtosis involves the mean of an even power of a variable, it does not distinguish, for instance, a deep trough (negative) from a sharp crest (positive) for $\eta$. It should be noticed that the effects of de-shoaling process on spatial evolution of kurtosis are different for the five variables. No significant enhancement of $\lambda_4(-w_t(z_0))$ and $\lambda_4(\eta)$ is observed in R3-step case. On the contrary, kurtosis of $u_t(z_0)$, $w(z_0)$, $u(z_0)$ are increased in the extended shallower region of R3-step case. Combined with the behaviour of skewness for these variables in the same region, we know that the increase of kurtosis is due to more negative extreme values (velocity or acceleration in the direction toward bottom). Regarding kurtosis, the most sensitive variable to the depth variation is again $w_t(z_0)$, whereas $\lambda_4(u(z_0))$ shows almost no change over the domain in R3-step case.

## 5. Discussion and conclusions

Basing on the recent experimental study of TRJR20, we studied the propagation of long-crested irregular waves over variable bottom profiles. With a fully nonlinear and dispersive numerical model, we first studied the case R3 with a submerged trapezoidal bar (R3-bar case) reported in TRJR20. Then, a variation of R3-bar case, with the

down-slope of the bar removed and the shallower flat region extended to the end of the domain, was considered (R3-step case). The main objective was to investigate the spectral adaptation and out-of-equilibrium dynamics of the sea-state due to depth transitions, and the associated statistics of the wave field.

The simulation of the R3-bar case not only validated the numerical model but also permitted extracting more information of the wave field, i.e. vertical velocity and accelerations at the elevation $z_0 = -0.048$ m (below SWL). The sea-state dynamics in R3 case was analysed in-depth by considering the spatial evolution of wave spectrum, bispectrum, eight non-dimensional parameters, distributions of $\eta$ and $H$ and statistics of kinematics. Additional simulations of the R3-bar case with different initial phases of the incident waves were conducted in order to apply the four-phase harmonic extraction approach, which allows evaluating the contributions of different harmonics in a quantitative manner. The simulation of R3-step case was then conducted, the effects of the de-shoaling process induced by the down-slope could be characterised by comparing with the R3-bar case.

As a first conclusion, the performance of whispers3D model was proven excellent in the deterministic simulation of irregular non-breaking wave train evolution over a long duration (equivalent to nearly $5,000T_p$). In all considered aspects, the comparisons with measurements showed good to outstanding agreement. This includes in particular the statistical distributions of wave heights, where the intensified extreme wave activities were successfully captured by the model. Nevertheless, some minor differences between the simulation and experiment exist. In the simulation, higher levels of significant wave height and steepness parameter after the shallower region, and slightly higher magnitudes of LF modes in the same area were observed. Both bispectrum and harmonic extraction results indicated that the LF modes in the simulation were generated due to second-order difference interaction. It is anticipated for a more energetic sea-state, the nonlinear wave-wave interaction is stronger resulting in more significant energy transfer to both LF modes and higher harmonics of the spectral peak. In the experiment, the wave train was of slightly lower energy after the shallower region than in the simulation due to frictional dissipation effects. The inclusion of dissipation in the model could bring some improvement, at least for the agreement of $H_{m_0}$.

The sea-state evolution of R3-bar case has been characterised and analysed thoroughly. In addition to the skewness and kurtosis evolution, we have observed a particular spatial modulation for nonlinear parameters ($H_{m_0}$, $H_{m_0}/\hat{L}_p$), spectral parameters ($Q_p$, $\hat{f}_p$), and B-F index, completing the analyses reported in TRJR20. The bispectral analysis, and harmonic extraction method permitted to characterise the spectral adaptation in terms of nonlinear interaction. Strong nonlinear coupling was detected, with significant energy transfer among the primary, second harmonics, third harmonics and long-wave components after the shoal. The contributions of these components to the evolution of wave spectrum, skewness and kurtosis have been evaluated by the harmonic extraction technique. Second-order effects were shown to be amplified after the shoaling zone, resulting in the generation of marked second harmonics (due to second-order sum interaction) and long-wave components (due to second-order difference interaction). The former dominated the evolution of $\lambda_3(\eta)$ and resulted in the enhancement of $\lambda_4(\eta)$, whereas the latter resulted in decrease of both parameters. Third harmonics of the primary components were noticeable only over the shallower region, with relatively low levels of energy. Yet their contribution to the kurtosis was evidenced, in particular regarding its maximum value after the length of latency (here equal to about half the local wavelength at peak frequency).

The empirical distributions of $\eta$ and wave height $H$ showed considerable deviation from Gaussianity (represented by the asymptotic model by Boccotti (2000) for $H$)

over the shallower region, with several freak waves occurring in the area where $\lambda_4(\eta)$ was close to its maximum. After the down-slope, the deviation from Gaussian models decreased, but the secondary peak close to the second harmonic in the spectrum did not vanish completely. The spectral changes due to a shoaling area are not fully reversible by setting a symmetric de-shoaling area, some wave energy remained in higher-order harmonics. A more complete statistical analysis of the kinematic properties, including free surface elevation, asymmetry parameter, velocities and accelerations components was performed. We found two different trends for the evolution of skewness of these variables, indicating that the deformations of the wave field take place somewhat independently in horizontal and vertical directions. The kurtosis of all the kinematic variables shown but the horizontal velocity (the single one considered in TRJR20) were enhanced, at the same position as $\lambda_4(\eta)$.

The comparison of the R3-bar case with the additional R3-step case allowed to isolate the effects induced by the de-shoaling process. In R3-step case, a particular beating pattern observed for $f > 1.6f_p$ in the range $x > 1.6$ m has been explained by the simultaneous presence of free and bound components in the high-frequency range. It also explains the similar but less pronounced (due to de-shoaling) spectral evolution pattern in R3-bar case. With the R3-step case, it is evident that the small spatial modulations of nonlinear and spectral parameters observed in R3-bar case were due to the de-shoaling process. The de-shoaling process influences the upstream wave field by forcing reflected waves.

In the R3-step case, the statistics of the kinematic variables continued their evolution trends over a short distance in the extended shallower region, then mildly varied until the end of the domain. The shallow-water equilibrium was thus not achieved over the shallower region in R3-bar case, nor is it fully achieved in the R3-step case. The comparison of the skewness and kurtosis in two cases demonstrated that the de-shoaling process affects the skewness of all variables oppositely compared to shoaling. Meanwhile the kurtosis of $u(z_0)$, $w(z_0)$ and $u_t(z_0)$ were enhanced due to de-shoaling.

The knowledge of the "transition water depth" for different dynamic sea-state responses, and the length of latency in the "shallower regime" case are of practical interest, since they are related to whether and in which range should a nearshore structure be protected from depth variation induced freak waves. Next, effort will be made in to improve our knowledge of these properties basing on information about seabed profile and incident spectrum. In complement to experiments, the nonlinear and dispersive whispers3D model will be used for this purpose, based on the accuracy of simulations reported here.

## Acknowledgements

Financial support provided by China Scholarship Council (CSC) to fund the Ph.D. research program of J. Zhang (grant No.201604490045) is gratefully acknowledged. We thank K. Trulsen, A. Raustøl, S. Jorde and L.B. Rye for selflessly sharing the experimental data of Run 3 of TRJR20. We also express our gratitude to three anonymous reviewers for their comments and suggestions that helped to improve this article.

## Declaration of interests

The authors report no conflict of interest.

## Appendix A. Statistical, spectral and bispectral analysis approaches

### A.1. *Characteristic non-dimensional parameters*

The skewness $\lambda_3$ and kurtosis $\lambda_4$ are defined as the third- and fourth-order normalised moments of a time series. The time series in the present work could be the surface elevation, velocity or acceleration in the horizontal or vertical directions. Using the free surface elevation $\eta$, their definitions are:

$$\lambda_3(\eta) = \left\langle (\eta - \langle\eta\rangle)^3 \right\rangle / \sigma^3, \quad \lambda_4(\eta) = \left\langle (\eta - \langle\eta\rangle)^4 \right\rangle / \sigma^4. \tag{A 1}$$

The peakedness parameter $Q_p$ characterising the spectral shape is defined as (see Goda 2010, p. 391):

$$Q_p = \frac{2}{m_0^2} \int_0^\infty f S^2(f)\, \mathrm{d}f. \tag{A 2}$$

Note that narrower the spectrum is, the larger $Q_p$ will be.

The parameter $\hat{f}_p$ is an estimate of the local peak frequency proposed by Young (1995):

$$\hat{f}_p = \left( \int_0^\infty f S^4(f)\, \mathrm{d}f \right) / \left( \int_0^\infty S^4(f)\, \mathrm{d}f \right). \tag{A 3}$$

The corresponding angular frequency is denoted as $\hat{\omega}_p$, the local wave-number and wavelength obtained through the linear dispersion relation are denoted $\hat{k}_p$ and $\hat{L}_p$ respectively.

The B–F index originally introduced in the work of Janssen (2003) plays an important role in understanding the effects of non-resonant four-wave interaction, its formulation reads:

$$\mathrm{BFI}_{J03} = \frac{\hat{k}_p \sqrt{2}\sigma}{\delta / \hat{\omega}_p}, \tag{A 4}$$

where $\delta$ denotes the width of the frequency spectrum.

The variation and robustness of B–F index with different parameters estimation approaches have been discussed by Olagnon & Magnusson (2004) and Serio *et al.* (2006). For uni-directional waves in constant water depth $h$, the threshold of modulation instability is $k_p h = 1.363$. When waves are modulationally unstable with $k_p h > 1.363$, it is suggested to use the formulation given by Serio *et al.* (2006) for single-peaked spectra:

$$\mathrm{BFI}_{S06} = \sqrt{m_0} \hat{k}_p Q_p \sqrt{2\pi} \nu \sqrt{\frac{|\beta|}{\alpha}}, \tag{A 5}$$

where $\alpha$, $\beta$ and $\nu$ are coefficients of the cubic NLS equation which was derived from equations (2.2–2.5) by using the method of multiple scales (Hasimoto & Ono 1972; Mei 1992):

$$-i \left( \frac{\partial A}{\partial t} + \frac{1}{2} \nu \frac{\omega}{k} \frac{\partial A}{\partial x} \right) + \alpha \frac{\partial^2 A}{\partial x^2} + \beta |A|^2 A = 0, \tag{A 6}$$

where $A(x,t)$ denotes the wave amplitude, $i$ denotes the imaginary unit, $\nu$ is the correction to the group velocity for finite depth, $\alpha$ and $\beta$ are the dispersive and nonlinear coefficients respectively:

$$\nu = \frac{2C_g}{C} = 1 + \frac{2kh}{\sinh(2kh)}, \tag{A 7}$$

$$\alpha = -\frac{1}{2}\frac{\mathrm{d}^2\omega(k)}{\mathrm{d}k^2} = \frac{\omega h}{2k}\left[\frac{1}{4kh} - \frac{kh}{\sinh^2(2kh)} - \frac{1-2kh\coth(2kh)}{\sinh(2kh)}\right], \tag{A 8}$$

$$\beta = \frac{\omega k^2\left(8+\cosh(4kh)-2\tanh^2(kh)\right)}{16\sinh^4(kh)} - \frac{\omega\left(2\omega\cosh^2(kh)+kC_g\right)^2}{2\sinh^2(2kh)\left(gh-C_g^2\right)}. \tag{A 9}$$

For $k_p h < 1.363$, the four-wave interaction vanishes due to the generation of a wave-induced mean flow. Hence, in such cases, waves are stabilised and another form of B–F index is recommended by Janssen & Onorato (2007):

$$B_s^2 = -\mathrm{BFI}_{J03}^2\,\frac{C_g^2}{C^2}\,\frac{gT_{0,0,0,0}}{k^4\omega}\left(\frac{\mathrm{d}^2\omega}{\mathrm{d}k^2}\right)^{-1}, \tag{A 10}$$

where $C = \omega/k$ is the phase velocity. $T_{0,0,0,0}$ is a known interaction coefficient with a complicated expression in the general case. Here, only its narrow-band limit is given:

$$\frac{T_{0,0,0,0}}{k^3} = \frac{9\tanh^4(kh) - 10\tanh^2(kh) + 9}{8\tanh^3(kh)} - \frac{1}{kh}\left[\frac{(4C_g - C)^2}{4\left(gh - C_g^2\right)} + 1\right]. \tag{A 11}$$

With the computation method (A 5) taken into account, we consider the B–F index in the cases with $k_p h < 1.363$ as:

$$B_s = \mathrm{BFI}_{S06}\,\frac{C_g}{C}\sqrt{\frac{gT_{0,0,0,0}}{2\alpha k^4\omega}}. \tag{A 12}$$

In the deep-water limit, $\alpha \to g/(8k\omega)$ and $T_{0,0,0,0} \to k^3$, $B_s$ reduces to $\mathrm{BFI}_{S06}$. In this study, the coefficients in both two definitions were evaluated using the local peak frequency $\hat{f}_p$.

### A.2. *Spectral and bispectral analyses*

The variance density spectrum is obtained by using Welch's method, with 50% overlapping rate of each $2^{14}$-point signal segment.

The bispectrum, introduced by Hasselmann *et al.* (1963), characterises the phase-coupling of 3 wave components due to nonlinear interactions. The triad-wave interactions result in wave energy transfer among $f_1$, $f_2$, and $f_1 + f_2$. In the present study we follow the definition of bispectrum $B(f_1, f_2)$ in Kim & Powers (1979):

$$B(f_1, f_2) = \left\langle X_1 X_2 X_{1+2}^* \right\rangle, \tag{A 13}$$

which is ensemble average of the triple product of complex Fourier coefficients, $X_i$ denotes the Fourier coefficient of frequency $f_i$, and the asterisk indicates complex conjugate.

In general, the bispectrum $B(f_1, f_2)$ is a complex quantity. The energy transfer direction is indicated by the sign of $\mathrm{Im}\{B(f_1, f_2)\}$, where $\mathrm{Im}\{\cdot\}$ means taking the imaginary part: negative values mean wave energy is transferred from the component $f_1 + f_2$ to $f_1$ and $f_2$ (difference interaction), positive values mean wave energy is transferred from $f_1$ and $f_2$ to $f_1 + f_2$ (sum interaction). As a measure of the horizontal asymmetry of the wave profile, the asymmetry parameter can be evaluated following Elgar & Guza (1985):

$$\text{Asymmetry} = \frac{\sum\sum \mathrm{Im}\left\{B\left(f_1, f_2\right)\right\}}{\sigma^3}, \tag{A 14}$$

The commonly used normalisation measure of bispectrum is the bicoherence:

$$b^2(f_1, f_2) = \frac{|B(f_1, f_2)|^2}{\langle |X_1 X_2|^2 \rangle \langle |X_{1+2}|^2 \rangle}. \tag{A 15}$$

The bicoherence $b^2(f_1, f_2)$, bounded in $[0, 1]$, is a measure of the relative strength of the coupling of the three wave components $f_1$, $f_2$, and $f_1 + f_2$. For instance, $b^2(f_1, f_2) = 1$ denotes total phase coupling, on the contrary, $b^2(f_1, f_2) = 0$ means the uncorrelated (random) phases.

### A.3. *Statistical distributions of surface elevation and wave heights*

The statistical distributions of the free surface elevation and individual wave heights are compared with linear theoretical expectations. Consider the free surface elevation $\eta$ is the sum of a large number of harmonic waves, each with a constant amplitude and a random phase, then the sea-state is a stationary, Gaussian process. The statistical characteristics are fully described by the variance density spectrum. The high-order moments are then: $\lambda_3(\eta) = 0$ and $\lambda_4(\eta) = 3$. The Gaussian distribution is expressed as (see e.g. Longuet-Higgins 1952):

$$p(\eta) = \frac{1}{\sigma\sqrt{2\pi}} \exp\left(-\frac{\eta^2}{2\sigma^2}\right), \tag{A 16}$$

where $p$ denotes the probability distribution function (PDF). However, it is known that nonlinear finite water effects have great influence on the statistics of the sea-state, causing considerable deviation from the Gaussian model, see the pioneering work of Bitner (1980).

In a Gaussian sea-state with a sufficiently narrow spectrum, the heights of wave crests are Rayleigh distributed. The crest-to-trough wave height could be approximated by twice of the crest height, thus it approximately follows Rayleigh distribution. However, such an assumption is not appropriate for sea-states with finite spectral width, leading to an overestimation of the probability of the high waves (see e.g. Forristall 1978). The wave height distribution models considering spectral width have been studied in, for instance, Naess (1985) and Boccotti (2000). Given that the JONSWAP spectrum with $\gamma = 3.3$ considered in the present study is not sufficiently narrow, the asymptotic model proposed by Boccotti (2000) is chosen as the reference distribution of wave heights:

$$P(H) = \frac{1 + b}{\sqrt{2b\,(1 + a)}} \exp\left(-\frac{H^2}{4\,(1 + a)}\right), \tag{A 17}$$

where $P(H)$ denotes the complementary cumulative distribution function (CCDF), $a$ and $b$ are evaluated as:

$$a = \left| \int_0^\infty S(f) \cos\left(2\pi f \tau^*\right) \mathrm{d}f \right| / m_0, \quad b = \left| \int_0^\infty f^2 S(f) \cos\left(2\pi f \tau^*\right) \mathrm{d}f \right| / m_2, \tag{A 18}$$

with $\tau^*$ denoting the time-lag of the global minimum of the autocorrelation function $\rho(\tau) = \langle \eta(t)\eta(t + \tau) \rangle$, and $m_2$ the second moment of the variance spectrum.

## REFERENCES

Baldock, T. E., Swan, C. & Taylor, P. H. 1996 A laboratory study of nonlinear surface waves on water. *Phil. Trans. R. Soc. A.* **354**, 649–676.

Beji, S. & Battjes, J. A. 1993 Experimental investigation of wave propagation over a bar. *Coastal Eng.* **19**, 151–162.

Belibassakis, K. A. & Athanassoulis, G. A. 2011 A coupled-mode system with application

to nonlinear water waves propagating in finite water depth and in variable bathymetry regions. *Coast. Eng.* **58**, 337–350.

Benjamin, T. B. & Feir, J. E. 1967 The disintegration of wave trains on deep water Part 1. Theory. *J. Fluid Mech.* **27**, 417–430.

Bingham, H. B. & Agnon, Y. 2005 A Fourier-Boussinesq method for nonlinear water waves. *Eur. J. Mech. B/Fluids* **24**, 255–274.

Bingham, H. B., Madsen, P. A. & Fuhrman, D. R. 2009 Velocity potential formulations of highly accurate Boussinesq-type models. *Coast. Eng.* **56**, 467–478.

Bitner, E. M. 1980 Non-linear effects of the statistical model of shallow-water wind waves. *Appl. Ocean Res.* **2**, 63–73.

Boccotti, P. 2000 *Wave Mechanics for Ocean Engineering*. Elsevier Science, Oxford.

Borthwick, A. G., Hunt, A. C., Feng, T., Taylor, P. H. & Stansby, P. K. 2006 Flow kinematics of focused wave groups on a plane beach in the U.K. coastal research facility. *Coast. Eng.* **53**, 1033–1044.

Chapalain, G., Cointe, R. & Temperville, A. 1992 Observed and modeled resonantly interacting progressive water-waves. *Coast. Eng.* **16**, 267–300.

Chen, H., Tang, X., Zhang, R. & Gao, J. 2018 Effect of bottom slope on the nonlinear triad interactions in shallow water. *Ocean Dyn.* **68**, 469–483.

Dommermuth, D. 2000 The initialization of nonlinear waves using an adjustment scheme. *Wave Motion* **32**, 307–317.

Ducrozet, G. & Gouin, M. 2017 Influence of varying bathymetry in rogue wave occurrence within unidirectional and directional sea-states. *J. Ocean Eng. Mar. Energy* **3**, 309–324.

Dysthe, K., Krogstad, H. E. & Müller, P. 2008 Oceanic rogue waves. *Annu. Rev. Fluid Mech.* **40**, 287–310.

Elgar, S. & Guza, R. T. 1985 Observations of bispectra of shoaling surface gravity waves. *J. Fluid Mech.* **161**, 425–448.

Fitzgerald, C. J., Taylor, P. H., Taylor, R. E., Grice, J. & Zang, J. 2014 Phase manipulation and the harmonic components of ringing forces on a surface-piercing column. *Proc. R. Soc. A* **470**, 20130847.

Forristall, G. Z. 1978 On the statistical distribution of wave heights in a storm. *J. Geophys. Res.* **83**, 2353.

Goda, Y. 2010 *Random seas and design of maritime structures (3rd edition)*. World Scientific Publishing Company.

Gottlieb, S. 2005 On high order strong stability preserving Runge-Kutta and multi step time discretizations. *J. Sci. Comput.* **25**, 105–128.

Gouin, M., Ducrozet, G. & Ferrant, P. 2016 Development and validation of a non-linear spectral model for water waves over variable depth. *Eur. J. Mech. B. Fluids* **57**, 115–128.

Gramstad, O., Zeng, H., Trulsen, K. & Pedersen, G. K. 2013 Freak waves in weakly nonlinear unidirectional wave trains over a sloping bottom in shallow water. *Phys. Fluids* **25**, 122103.

Hasimoto, H. & Ono, H. 1972 Nonlinear modulation of gravity waves. *J. Phys. Soc. Jpn.* **33**, 805–811.

Hasselmann, K., Munk, W. & MacDonald, G. 1963 *Bispectra of ocean waves. In: M. Rosenblatt Time Series Analysis*. New York: John Wiley.

Janssen, P. A. E. M. 2003 Nonlinear four-wave interactions and freak waves. *J. Phys. Oceanogr.* **33**, 863–884.

Janssen, P. A. E. M. & Onorato, M. 2007 The intermediate water depth limit of the Zakharov equation and consequences for wave prediction. *J. Phys. Oceanogr.* **37**, 2389–2400.

Kashima, H., Hirayama, K. & Mori, N. 2014 Estimation of freak wave occurrence from deep to shallow water regions. *Coast. Eng. Proc.* **1**, 36.

Kashima, H. & Mori, N. 2019 Aftereffect of high-order nonlinearity on extreme wave occurrence from deep to intermediate water. *Coast. Eng.* **153**, 103559.

Katsardi, V., de Lutio, L. & Swan, C. 2013 An experimental study of large waves in intermediate and shallow water depths. Part I: Wave height and crest height statistics. *Coast. Eng.* **73**, 43–57.

Kharif, C. & Pelinovsky, E. 2003 Physical mechanisms of the rogue wave phenomenon. *Eur. J. Mech. B/Fluids* **22**, 603–634.

Kim, Y. C. & Powers, E. J. 1979 Digital bispectral analysis and its applications to nonlinear wave interactions. *IEEE T. Plasma Sci.* **7**, 120–131.

Le Méhauté, B. 1976 *An Introduction to Hydrodynamics and Water Waves*. Springer Berlin Heidelberg.

Longuet-Higgins, M. S. 1952 On the statistical distribution of the height of sea waves. *J. Mar. Res.* **11**, 245–265.

Ma, Y., Ma, X. & Dong, G. 2015 Variations of statistics for random waves propagating over a bar. *J. Mar. Sci. Technol.* **23**, 864–869.

Madsen, P. A., Fuhrman, D. R. & Wang, B. 2006 A Boussinesq-type method for fully nonlinear waves interacting with a rapidly varying bathymetry. *Coast. Eng.* **53**, 487–504.

Mansard, E. P. D. & Funke, E. R. 1980 The measurement of incident and reflected spectra using a least squares method. In *Coastal Engineering 1980*, pp. 154–172.

Massel, S. R. 1983 Harmonic generation by waves propagating over a submerged step. *Coast. Eng.* **7**, 357–380.

Mei, C. C. 1992 *The Applied Dynamics of Ocean Surface Waves*. World Scientific Publishing Company.

Mori, N. & Janssen, P. A. E. M. 2006 On kurtosis and occurrence probability of freak waves. *J. Phys. Oceanogr.* **36**, 1471–1483.

Naess, A. 1985 On the distribution of crest to trough wave heights. *Ocean Eng.* **12**, 221–234.

Olagnon, M. & Magnusson, A. K. 2004 Sensitivity study of sea state parameters in correlation to extreme wave occurrences. In *Proc. 14th Int. Offshore and Polar Engineering Conf. (ISOPE), 23-28 May, Toulon, France*.

Onorato, M., Osborne, A. R. & Serio, M. 2005 Modulational instability and non-Gaussian statistics in experimental random water-wave trains. *Phys. Fluids* **17**, 078101.

Papoutsellis, C. E., Charalampopoulos, A. G. & Athanassoulis, G. A. 2018 Implementation of a fully nonlinear Hamiltonian coupled-mode theory, and application to solitary wave problems over bathymetry. *Eur. J. Mech. B. Fluids* **72**, 199–224.

Raoult, C., Benoit, M. & Yates, M. L. 2016 Validation of a fully nonlinear and dispersive wave model with laboratory non-breaking experiments. *Coast. Eng.* **114**, 194–207.

Sergeeva, A., Pelinovsky, E. & Talipova, T. 2011 Nonlinear random wave field in shallow water: variable Korteweg-de Vries framework. *Nat. Hazards Earth Syst. Sci.* **11**, 323–330.

Serio, M., Onorato, M., Osborne, A. R. & Janssen, P. A. E. M. 2006 On the computation of the Benjamin–Feir index. *Il Nuovo Cimento C* **28**, 893–903.

Simon, B., Papoutsellis, C. E., Benoit, M. & Yates, M. L. 2019 Comparing methods of modeling depth-induced breaking of irregular waves with a fully nonlinear potential flow approach. *J. Ocean Eng. Mar. Energy* **5**, 365–383.

Tian, Y. & Sato, S. 2008 A numerical model on the interaction between nearshore nonlinear waves and strong currents. *Coast. Eng. J.* **50**, 369–395.

Toffoli, A., Fernandez, L., Monbaliu, J., Benoit, M., Gagnaire-Renou, E., Lefèvre, J. M., Cavaleri, L., Proment, D., Pakozdi, C., Stansberg, C. T., Waseda, T. & Onorato, M. 2013 Experimental evidence of the modulation of a plane wave to oblique perturbations and generation of rogue waves in finite water depth. *Phys. Fluids* **25**, 091701.

Trulsen, K., Raustøl, A., Jorde, S. & Rye, L. B. 2020 Extreme wave statistics of long-crested irregular waves over a shoal. *J. Fluid Mech.* **882**, R2.

Trulsen, K., Zeng, H. & Gramstad, O. 2012 Laboratory evidence of freak waves provoked by non-uniform bathymetry. *Phys. Fluids* **24**, 097101.

Viotti, C. & Dias, F. 2014 Extreme waves induced by strong depth transitions: fully nonlinear results. *Phys. Fluids* **26**, 051705.

Yates, M. L. & Benoit, M. 2015 Accuracy and efficiency of two numerical methods of solving the potential flow problem for highly nonlinear and dispersive water waves. *Int. J. Numer. Methods Fluids* **77**, 616–640.

Young, I.R. 1995 The determination of confidence limits associated with estimates of the spectral peak frequency. *Ocean Eng.* **22**, 669–686.

Zakharov, V. E. 1968 Stability of periodic waves of finite amplitude on the surface of a deep fluid. *J. Appl. Mech. Tech. Phys.* **9**, 190–194.

Zang, J., Gibson, R., Taylor, P. H., Taylor, R. Eatock & Swan, C. 2006 Second order

wave diffraction around a fixed ship-shaped body in unidirectional steep waves. *J. Offshore Mech. Arct. Eng.* **128**, 89–99.

Zang, J., Taylor, P. H., Morgan, G., Tello, M., Grice, J. & Orszaghova, J. 2010 Experimental study of non-linear wave impact on offshore wind turbine flundations. In *Coastlab10: 3rd Int. Conf. on the Application of Physical Modelling to Port and Coastal Protection, 28th Sep.–1st Oct., Barcelona, Spain*.

Zeng, H. & Trulsen, K. 2012 Evolution of skewness and kurtosis of weakly nonlinear unidirectional waves over a sloping bottom. *Nat. Hazards Earth Syst. Sci.* **12**, 631–638.

Zhang, J., Benoit, M., Kimmoun, O., Chabchoub, A. & Hsu, H.-C. 2019 Statistics of extreme waves in coastal waters: large scale experiments and advanced numerical simulations. *Fluids* **4**, 99.

Zheng, Y., Lin, Z., Li, Y., Adcock, T. A. A., Li, Y. & van den Bremer, T. S. 2020 Fully nonlinear simulations of unidirectional extreme waves provoked by strong depth transitions: The effect of slope. *Phys. Rev. Fluids* **5**, 064804.